Catalytic Activity Maps for Alloy Nanoparticles

Liang Cao[1, 2], Tim Mueller[2,*]

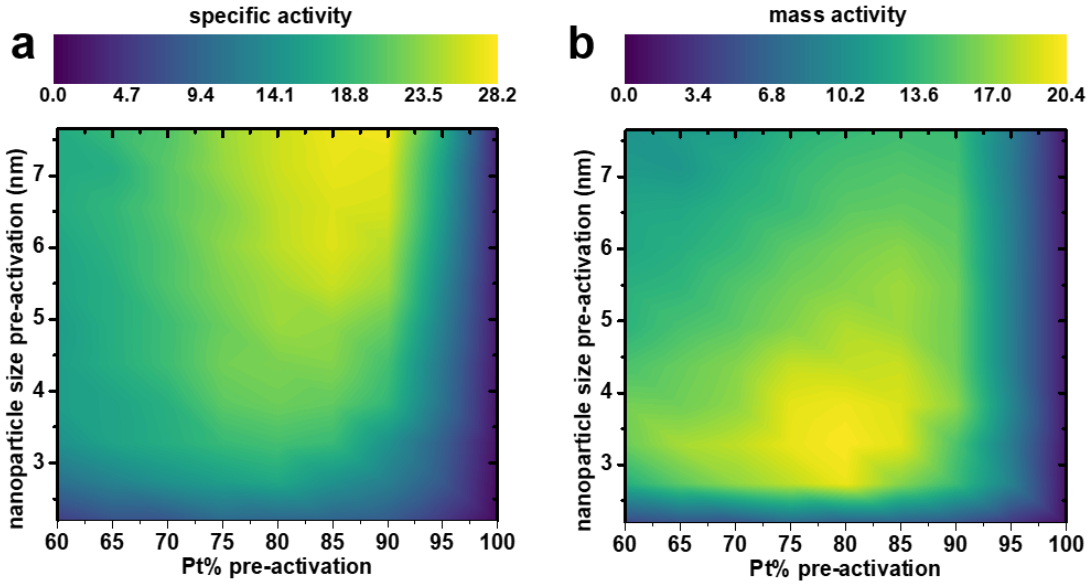

[1]Department of Chemistry, Zhejiang University, Hangzhou, Zhejiang 310000, P. R. China

[2]Department of Materials Science and Engineering, Johns Hopkins University, Baltimore, Maryland 21218, United States

*Corresponding author(s): Tim Mueller (tmueller@jhu.edu)

Abstract

To enable rational design of alloy nanoparticle catalysts, we develop an approach to generate catalytic activity maps of alloy nanoparticles on a grid of particle size and composition. The catalytic activity maps are created by using a quaternary cluster expansion to explicitly predict adsorbate binding energies on alloy nanoparticles of varying shape, size, and atomic order while accounting for interactions among the adsorbates. This cluster expansion is used in kinetic Monte Carlo simulations to predict nanoparticle structures and turnover frequencies on all surface sites. We demonstrate our approach on Pt–Ni octahedral nanoparticle catalysts for the oxygen reduction reaction (ORR), revealing the nanoparticle size and composition predicted to maximize ORR activity.

Keywords: rational design, intermetallic, solid-solution, cluster expansion, density functional theory, Pt–Ni catalysts, oxygen reduction reaction

Introduction

Alloy nanoparticles are well suited to be catalysts due to their high surface to volume ratios and the abundance of ways in which the structures and properties of the catalysts can be tailored. Various experimental synthesis strategies (e.g., core-shell[1], doping[2, 3, 4], shape-engineering[5]) have been used to improve the catalytic activity and stability of alloy nanocatalysts, but to limit the number of costly and time consuming experiments that must be done there is great interest in rational nanocatalyst design. Unfortunately, computational design of alloy nanocatalysts remains a significant challenge due to their size and complexity. Density functional theory (DFT)[6] calculations in standard implementations scale with the number of valence electrons as $O(N^3)$,[7] limiting the diameter of nanoparticles that can be practically modelled to about 2–3 nm, below the typical diameters (4–10 nm) of particles evaluated experimentally.[2, 4, 5, 8, 9] In addition, the arrangement of atoms in a substitutional alloy can dramatically affect its catalytic properties,[10, 11] making the computational prediction of the atomic structure of the catalyst a critically important step in the design process. Predicting the structure of a substitutional nanoalloy either through thermodynamic[2, 12, 13, 14] or kinetic[3, 15, 16] modelling requires the evaluation of the energies of a large number of candidate structures, where the energy differences between competing alloy structures can be on the order of meV / atom.[17] The design of alloy nanocatalysts is further complicated by the need to accurately predict adsorbate binding energies, an important descriptor of catalytic activity, on a variety of possible adsorption sites.

Various approaches have been used to computationally predict the structures and properties of alloy nanocatalysts. One strategy is to study nanoparticles that are small enough (~2 nm in diameter) to be modeled using DFT.[2, 18, 19, 20] However the cost of DFT calculations limits the number of structures that can be evaluated this way, and this approach cannot in practice be used

to model particles of typical experimental sizes. Alternatively, nanoparticle facets may be approximated as extended surfaces, on which adsorbate binding energies can be calculated using DFT.[3, 11, 21, 22] The disadvantage of this approach is that it does not fully account for the variety of binding sites, including sites near edges and vertices, on a nanoparticle surface.

Due to the cost of directly using DFT, there has recently been significant interest in developing fast and accurate surrogate models for nanocatalysts. Calle-Vallejo et al.[23, 24] developed an approach in which the *OH and *OOH adsorption energies on Pt nanoparticles were linearly correlated with the generalized coordination number (GCN) of the surface binding site, which takes both the first- and second-nearest neighbors into account. Jinnouchi et al.[25] developed a machine-learned interatomic potential model based on the smooth overlap of atomic positions (SOAP) kernel[26] to predict structures, catalytic activities, and N, O, and NO adsorption energies for fixed-shape Au–Rh nanoparticles with varied sizes. For catalysts with structures that can be mapped to a lattice model (e.g., an fcc lattice), formation energies can be accurately calculated using cluster expansions.[2, 3, 13, 19, 20, 27] This approach can be extended to the calculation of adsorption energies by including coordination-number-dependent and metal-specific correction terms into DFT-parametrized cluster expansions[3, 15], or by explicitly including adsorbates in the cluster expansion as a separate species.[14]

Here we present the use of machine-learned cluster expansions to computationally screen nanocatalysts of experimentally relevant sizes and identify those that are expected to have high activity. We demonstrate this approach on Pt–Ni nanoparticle catalysts for the oxygen reduction reaction (ORR), which have been extensively studied as promising catalysts in fuel cells.[28] We use the adsorption energy of OH as a descriptor of catalytic activity, as it has been shown to be an accurate descriptor,[29, 30] and in operating conditions OH is likely to be the most prevalent species

on the alloy surface.[31] By explicitly including OH in the cluster expansion we realistically account for adsorbate-adsorbate interactions (See Methods). Catalytic activity is then predicted using kinetic Monte Carlo (KMC)[32, 33] simulations to calculate the turnover frequencies on all surface sites. Applying this approach to particles over a range of compositions and sizes yields catalytic activity maps for the ORR that indicate the optimal size, composition, and phase of the Pt–Ni nanoparticle catalysts for the ORR, an important step towards the rational design of alloy nanocatalysts.

Results and Discussions

We start by validating our approach for predicting activities against experimental data. Experimentally, the measured specific and mass activities of Pt–Ni nanocatalysts are usually referenced to those of state-of-the-art commercial Pt/C.[3, 5, 15] To simulate this reference state, we have calculated size-weighted activity averages according to the diameter length distribution of commercial Pt/C used in our previous work.[15] Based on the Wulff construction of Pt[14], we chose a truncated octahedron as the shape of Pt nanoparticles. Our KMC simulations predict the specific activity of the Pt(111) surface (Supplementary Table 3) to be about 3.8 times relative to that of commercial Pt/C, which is in good agreement with experiments (5 – 10 times).[34, 35] We further validated our approach for predicting catalytic activities by comparing experimentally measured and KMC-predicted activities for two representative Pt–Ni octahedral particles (***Table 1***).[3, 15] The simulated structures of these particles were matched to experimental data as described in reference.[3, 15] The comparison suggests that our approach slightly overestimates the activities of the Pt–Ni nanoparticles, relative to Pt/C, by a factor of about 1.3 – 1.7. The reason for this

overestimation may be the underestimation of the activity of the Pt/C reference state. More details on the specific activities of the Pt(111) surface and representative Pt–Ni(111) surfaces are provided in the Supplementary Information (Supplementary Table 3, and Supplementary Figs. 2 and 3).

Table 1. Validation of the approach for predicting activities of alloy nanoparticles. Comparison of the experimentally measured and KMC predicted specific and mass activities of two representative Pt–Ni octahedral particles. "before KMC" and "after KMC" mean before and after the simulation of Ni dissolution, respectively. The specific and mass activities were predicted on the snapshots of Pt–Ni particles after KMC (Ni dissolution). The experimental and predicted values are referenced to those of commercial Pt/C, respectively.

References	Pt–Ni octahedral particles		specific activity based on H_{upd}		mass activity	
	before KMC	after KMC	experiment	prediction	experiment	prediction
Jia et al.[15]	$Pt_{4495}Ni_{1680}$	$Pt_{4495}Ni_{895}$	10	16.90	6.88	11.03
Cao et al.[3]	$Pt_{4045}Ni_{2130}$	$Pt_{4045}Ni_{1078}$	13.33	17.65	9.29	12.67

To predict the catalytic activity of a nanoparticle it is first necessary to predict the nanoparticle structure. Pt–Ni nanoparticles used as ORR catalysts in proton exchange membrane (PEM) fuel cells typically start as disordered Pt–Ni solid solutions that achieve a Pt-rich shell through an activation process[3, 15] which is usually done by performing cyclic voltammetry (CV) in N_2-saturated 0.1 M $HClO_4$.[2, 3, 15] Under such acidic treatment, surface Ni oxides will dissolve and surface Pt/Ni atoms will migrate.[3, 15] To construct realistic nanoparticle structures, we initialize the particle a fully disordered solid solution and simulate the activation process using kinetic Monte Carlo (KMC)[32, 33], as described in our previous work.[3, 15] 6175-atom (~5.5 nm) nanoparticles with initial (pre-activated) Ni compositions of 40%, 30%, 20% and 10% lose about 40.0%, 34.9%, 31.2% and 28.0% of their Ni, respectively (Supplementary Fig. 4).

Once we have predicted the structure of a nanoparticle, we evaluate catalytic activities by using KMC to estimate the turnover frequency for each adsorbed OH. Specific and mass activities are then calculated by dividing the sum of turnover frequencies by the number of surface Pt atoms and the number of total Pt atoms, respectively. We construct catalytic activity maps (***Fig. 1***) by repeating this process on a grid with respect to composition and particle edge length (as determined by the pre-activated particles). At each point on this grid, we sample 10 structures to reduce noise introduced by the stochastic determination of the nanoparticle structure. The resulting catalytic activity maps for Pt–Ni octahedral nanoparticles (***Fig. 1***) reveal that specific activity increases with particle edge length and starts to plateau at an edge length of about 5.5 nm, reaching a maximal value of about 28 times that of Pt/C when the initial (pre-activated) nanoparticle has a composition of about $Pt_{0.85}Ni_{0.15}$(***Fig. 1***a). The mass activity is optimized at a composition of about $Pt_{0.8}Ni_{0.2}$ and an edge length of 3.3 nm – 3.8 nm (***Fig. 1***b).

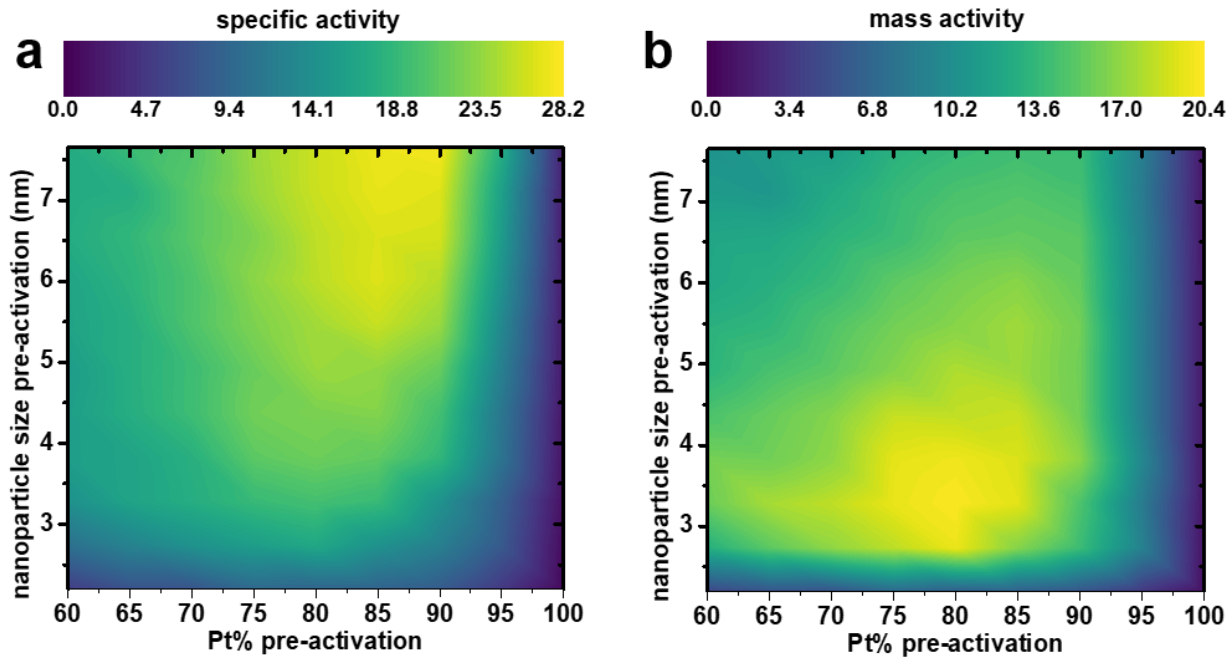

Fig. 1. Size-composition catalytic maps of disordered Pt–Ni nanoparticles. a Predicted specific activity of activated particles. **b** Predicted mass activity of activated particles. The x-axis is the Pt composition before KMC (pre-activation) with an increment of 5%, and the y-axis is the edge length before KMC. All specific and mass activity values are referenced to those of simulated commercial Pt/C (see details in section 5 of the Supplementary Information).

Comparison of our calculations to experimental results is challenging as there have been few systematic experimental studies on size and composition effects in Pt–Ni particles. Experimentally, the highest reported mass activity for Pt–Ni nanoparticles by Younan Xia et al.[36] is about 17 times that of Pt/C. This result was achieved on octahedral $Pt_{0.72}Ni_{0.28}$ particles with an edge length of about 9 nm, but results on other sizes and compositions were not reported in that work. The solvent used in the synthesis of the nanoparticles was found to change the mass activity by a factor of two, highlighting the importance of factors beyond size and composition in determining particle activity. Alonso-Vante et al. studied composition effects in nanoparticles with diameters of 2–3 nm.[37] The variation of particle size with composition among the samples complicates the analysis of mass activity, but specific activity was found to have a broad peak

around a composition of about $Pt_{0.7}Ni_{0.3}$. This is consistent with our prediction for 3.3 nm particles, which shows broad peaks with maximal activity at a composition of around $Pt_{0.8}Ni_{0.2}$ and only slightly less activity at a composition of $Pt_{0.7}Ni_{0.3}$ (Supplementary Fig. 5a). More recently, 4.5–7.5 nm (in edge length) Pt–Ni nanoparticles with a pre-activated composition of $Pt_{0.6}Ni_{0.4}$ were reported by Zhang et al. to be more active than particles with a pre-activated composition of $Pt_{0.75}Ni_{0.25}$.[38] The highest mass activity for the $Pt_{0.6}Ni_{0.4}$ particles was observed to occur for particles with an edge length of 5.8 nm, whereas the mass activity of the $Pt_{0.75}Ni_{0.25}$ nanoparticles showed relatively little change with particle size and was maximized for the largest particles. On the other hand, for pure Pt small nanoparticles (~2–3 nm in diameter) have been shown to maximize mass activity.[39, 40]

The size and composition at which we predict catalytic activity to be maximized are similar to those observed experimentally, but the experimental results suggest that peak activity occurs for nanoparticles with initial compositions that are more Ni-rich than those predicted by our models. This difference can be partially explained by the amount of Ni dissolution in the particles. For example, Zhang found that $Pt_{0.6}Ni_{0.4}$ nanoparticles with an edge length between 4.5 nm and 8.0 nm lost about 60% of the Ni in the particle after activation, but $Pt_{0.75}Ni_{0.25}$ nanoparticles with an edge length between 4.5 nm and 7.5 nm only lost about 25%.[38] As a result, the post-activated nanoparticles evaluated experimentally had nearly the same composition regardless of their initial compositions. In contrast, for disordered particles with an edge length of 5.5 nm our simulations predict 40% Ni loss for $Pt_{0.6}Ni_{0.4}$ and 32% Ni loss for $Pt_{0.75}Ni_{0.25}$. Thus the post-activated $Pt_{0.6}Ni_{0.4}$ nanoparticle has more Ni than the post-activated $Pt_{0.75}Ni_{0.25}$ nanoparticle, which weakens OH adsorption and leads to lower catalytic activity (Supplementary Fig. 6). Maps of predicted specific

and mass activities for Pt–Ni nanoparticles as a function of the post-activated composition of the nanoparticle are provided in Supplementary Fig. 7.

We have found that in pure Pt and Pt-rich (111) surfaces, density functional theory predicts sub-surface vacancies to be significantly more stable than surface vacancies, by about 0.5 – 1 eV (Supplementary Table 4). We believe this is likely related to reports that DFT significantly underpredicts bulk vacancy formation energies in Pt.[41, 42] Although this effect is less pronounced in the energies calculated using the cluster expansion, the nanoparticle structures generated by our KMC calculations had an unexpectedly high concentration of sub-surface vacancies below flat (111) surfaces (~0.1% as shown in Supplementary Fig. 8a). Most of the sub-surface Pt vacancies exist in the 2nd layer of the activated disordered particles. If this result is an artifact of errors inherent in DFT, the resulting over-stabilization of Pt-rich (111) surfaces provides a possible explanation for the apparent under-prediction of Ni dissolution.

There is evidence that the initial Pt concentration in Pt–Ni particles is greater near the particle edges,[5, 8] which may also explain the discrepancy between our predictions and experimental results. To investigate this possibility, we ran simulations on disordered Pt–Ni particles initialized with different degrees of Pt-rich edges. This process is described in detail in section 11 of the Supplementary Information. We observed little change in the composition that is predicted to maximize activity (Supplementary Fig. 9), indicating that the initial distribution of Pt and Ni atoms cannot fully explain the slight difference between our calculations and experiments.

The calculated catalytic activity maps provide insights into the atomic origins of catalytic activity trends for alloy nanoparticles. At a composition of $Pt_{0.85}Ni_{0.15}$, which is predicted to yield nearly optimal specific activity, the specific activity increases as the edge length increases from

2.1 nm to 5.5 nm, and then starts to plateau when the edge length is larger than 5.5 nm (***Fig. 2*****a**). This behavior can be largely attributed to the fraction of surface Pt atoms that are at sites with a coordination number of 9, denoted as Pt(111) sites(***Fig. 2*****a**). The average turnover frequencies are predicted to be maximized at these sites (**Fig. 3**b-e and **Fig. *4***e). The fraction of Pt(111) sites on the surface reaches a plateau of about 0.72 at an edge length of about 5.5 nm (***Fig. 2*****a**), with the remaining surface Pt atoms on edge sites, vertex sites, near step edges, or near sub-surface vacancies (***Fig. 3*****b**). This is in contrast to the expected behavior for an octahedral particle, in which the fraction of (111) sites should increase monotonically with particle size (***Fig. 2*****d**). This observation indicates that when the pre-activated edge length gets larger than about 5.5 nm, any size-dependent increase in the density of Pt(111) sites on the surface is offset by an increase in the density of step edges (or other defects) on the surfaces of activated particles (Supplementary Fig. 10). Other factors, such as the second-layer composition (Supplementary Figs. 10 and 11b, and Supplementary Table 6) are not as well correlated with specific activity.

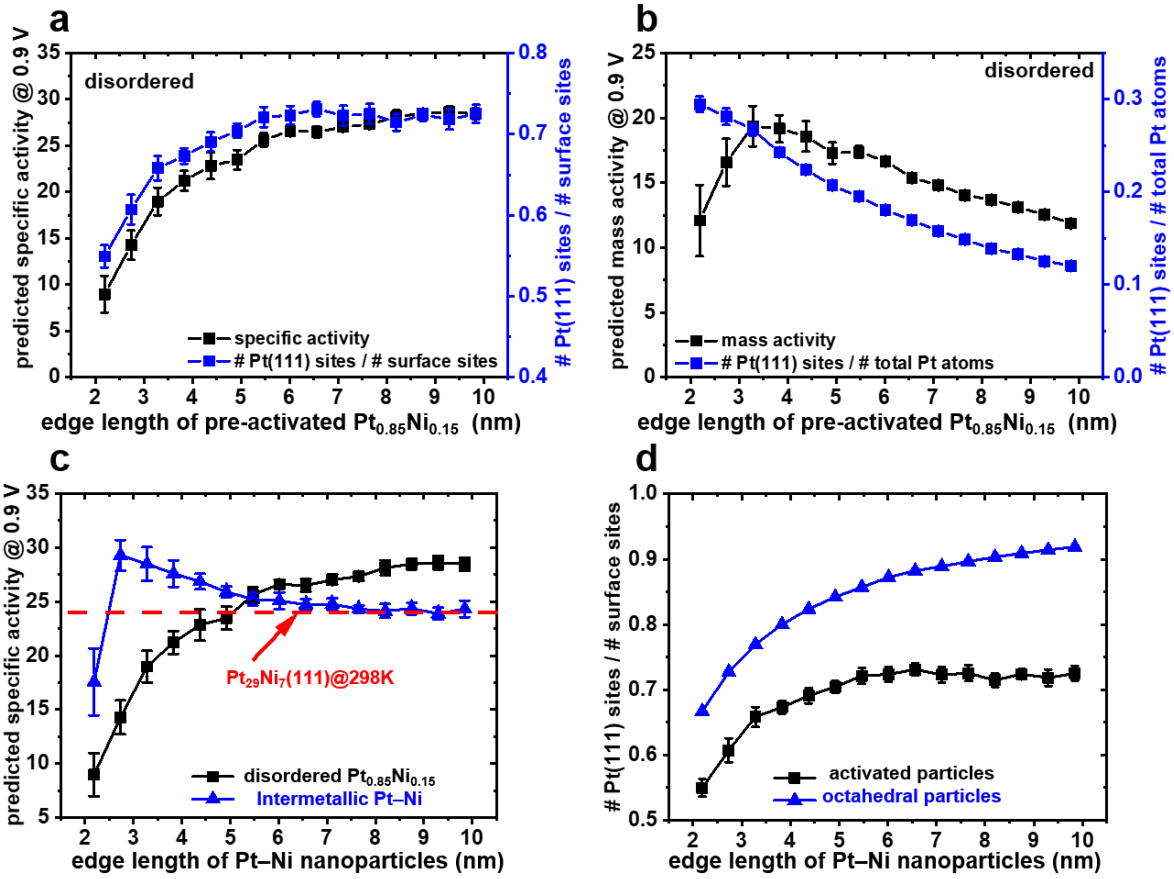

Fig. 2. Size effect on specific and mass activities of Pt–Ni particles. a Predicted specific activity and ratio of the number of surface Pt(111) sites (CN=9) to the number of total surface Pt atoms of disordered $Pt_{0.85}Ni_{0.15}$. **b** Predicted mass activity and ratio of the number of surface Pt(111) sites (CN=9) to the number of total Pt atoms of disordered $Pt_{0.85}Ni_{0.15}$. **c** Predicted specific activity of disordered $Pt_{0.85}Ni_{0.15}$ and intermetallic Pt–Ni particles at the Pt and Ni chemical potentials that maximize the specific activity of 5.5 nm particles. The red line represents the $Pt_{29}Ni_7$(111)@298K surface with 100%, 75%, 75%, and 75% in the first, second, third, and fourth layers.[12] **d** Ratio of the number of surface Pt(111) atoms to the number of total surface Pt atoms of activated disordered $Pt_{0.85}Ni_{0.15}$ (labeled as "activated particles") and octahedral particles. All specific activity and mass activity values are referenced to those of simulated commercial Pt/C.

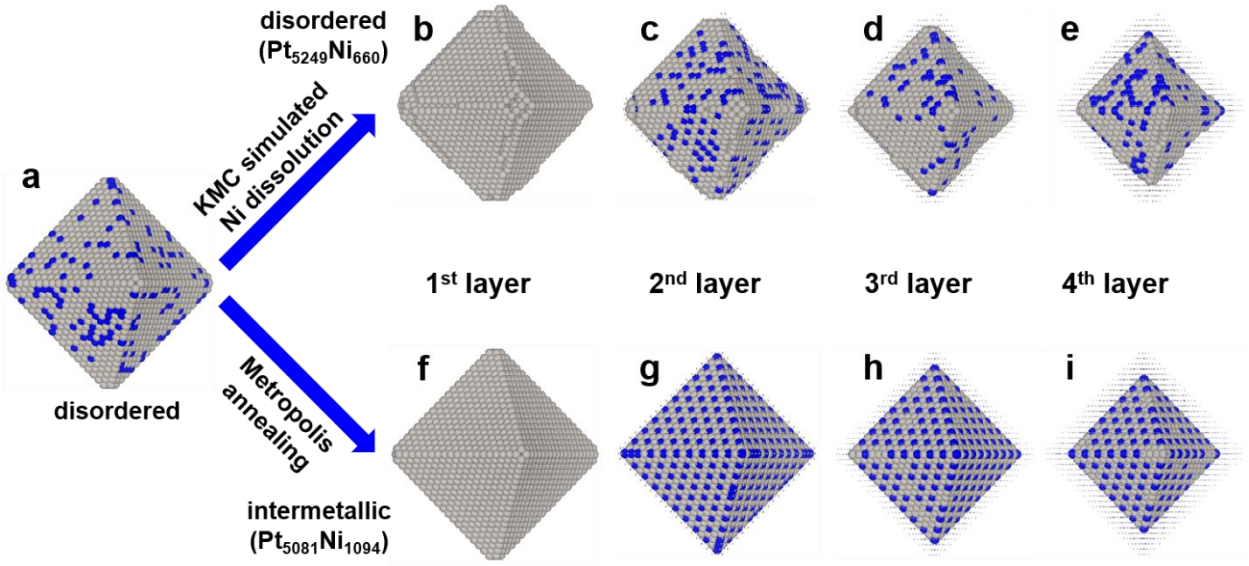

Fig. 3. Layer-by-layer snapshots of disordered and intermetallic Pt–Ni particles. a A snapshot of disordered $Pt_{0.85}Ni_{0.15}$ nanoparticle with randomly occupied Pt/Ni atoms. **b, c, d, e** The first (**b**), second (**c**), third (**d**), and fourth (**e**) layers of a snapshot of activated disordered $Pt_{0.85}Ni_{0.15}$ nanoparticle after KMC simulation of Ni dissolution and Pt/Ni migration at 298 K. **f, g, h, i** The first (**f**), second (**g**), third (**h**), and fourth (**i**) layers of a snapshot of intermetallic $Pt_{0.82}Ni_{0.18}$ nanoparticle after Metropolis Monte Carlo simulation at 298 K.

At the composition of $Pt_{0.85}Ni_{0.15,}$ mass activity is predicted to increase as the edge length increases from 2.2 nm to 3.3 nm, and then it decreases as the edge length increases further (***Fig. 2***b). The low mass activity at small sizes can be explained by the prediction that OH binding on Pt(111) sites becomes stronger at small particle sizes (Supplementary Fig. 12), consistent with DFT-calculated results that oxygen binding becomes stronger as the size of nanoparticle size decreases.[40] At larger sizes, the change in the of *OH binding energy slows,[43] and the ratio of surface Pt(111) sites to the number of total Pt atoms becomes a more important factor in determining the size-dependent mass activity, leading to decreased mass activity (**Fig. *2***b).

The highest reported specific activity for a Pt–Ni catalyst is on the extended $Pt_3Ni(111)$ surface [31], which is likely to be at least partially ordered in the thermodynamically stable $L1_2$ intermetallic phase.[44] We have thus also investigated an alternative hypothetical scenario, in which 2.2–9.9 nm

octahedral nanoparticles are initialized with thermodynamically stable atomic ordering as determined using Metropolis Monte Carlo simulations[45] (described in detail in section 14 of the Supplementary Information). The particles are estimated to maintain their octahedral shape due to their thermodynamic stability and the kinetic protection provided by the well-ordered Pt shell; this is supported by the fact that there is almost no Ni dissolution and shape change after running KMC on these intermetallic nanoparticles at 298 K. Within the chemical potential window in which bulk Pt_3Ni is stable, maximal specific and mass activities are achieved in intermetallic 6175-atom (~5.5 nm in the edge length) particles with a composition of about $Pt_{0.82}Ni_{0.18}$ (Supplementary Fig. 13a). These particles have an $L1_2$ core (**Fig. *3*f-i** and Supplementary Figs. 14 and 15) and a Pt monolayer skin, in good agreement with the bulk phase diagram[44, 46] and previous calculations.[2, 13] Although intermetallic $Pt_{0.82}Ni_{0.18}$ particles and disordered $Pt_{0.85}Ni_{0.15}$ nanoparticles both have a Pt skin (**Fig. *2***b, f), the activities of the intermetallic particles are much more sensitive to the overall particle composition than the activities of the disordered particles, as changes in the composition of the intermetallic particles largely occur through changes in the composition of the near-surface layers (Supplementary Fig.14 and Supplementary Table 7).

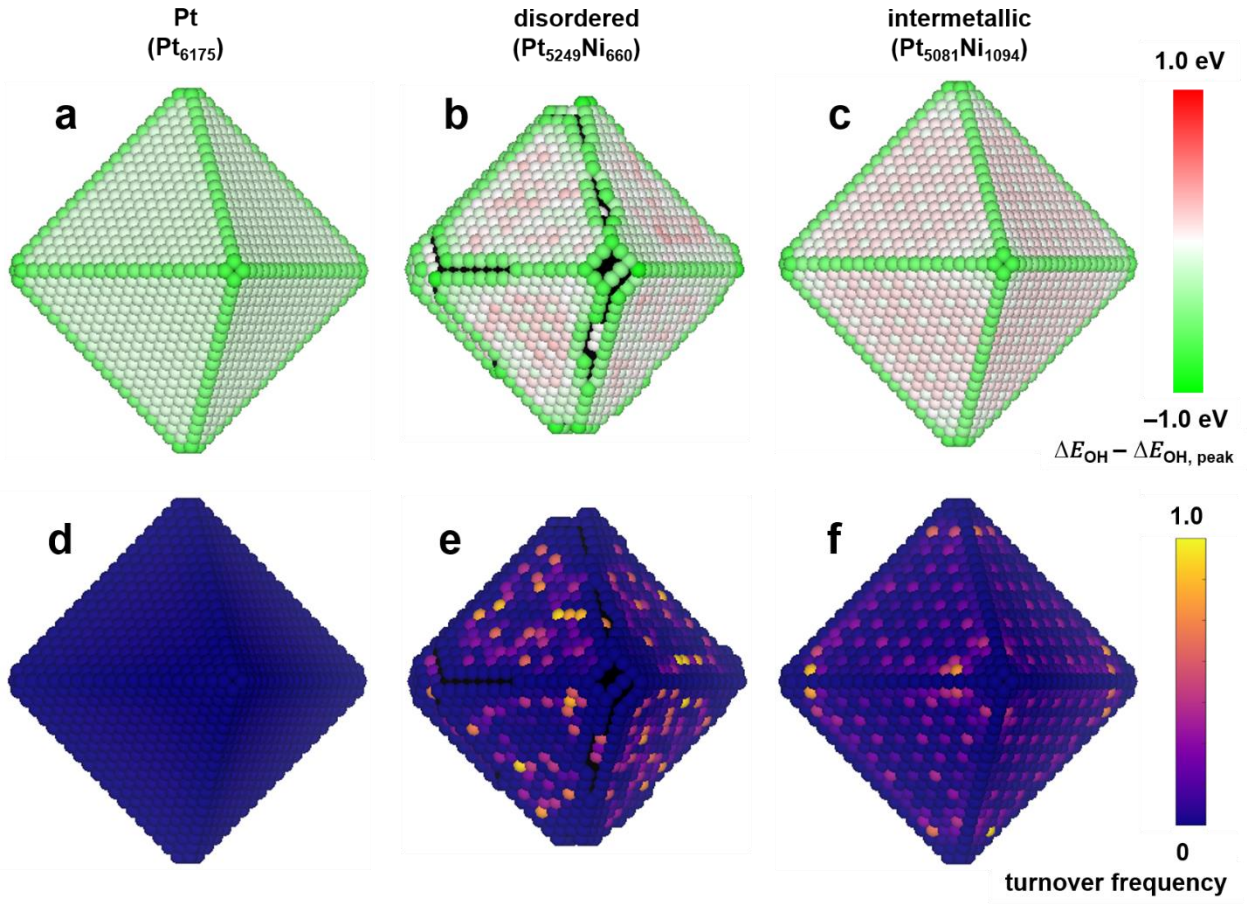

Fig. 4. Predicted *OH binding energy and turnover frequency. a, b, c The average *OH binding energy on each surface site of three representative nanoparticles with an edge length of ~5.5 nm: Pt (**a**), disordered $Pt_{0.85}Ni_{0.15}$ in **Fig. 3b-e** (**b**), and intermetallic $Pt_{0.82}Ni_{0.18}$ in **Fig. 3f-i** (**c**). **d, e, f** The corresponding average turnover frequency on each site. Binding energies and turnover frequencies referenced to those at the peak of the volcano plot are average values over the number of KMC recording steps, which are 15 times the number of surface Pt atoms. Corresponding histograms of binding energies and turnover frequencies are provided in Supplementary Figs. 19 and 20.

To investigate the size effect on specific and mass activities of intermetallic particles we set the chemical potential difference between Pt and Ni to that which maximizes activity in the 6175-atom particles, resulting in an ordered $L1_2$ structure at all subsurface layers for particles with edge length

larger than 3.3 nm (**Fig. *3*f-i** and Supplementary Fig. 15). For smaller particles, similar atomic structures have been observed but with slightly lower Pt content in sub-surface layers (Supplementary Fig. 16 and Supplementary Table 8). The predicted specific activity and mass activity of intermetallic particles reaches a maximum value at about 2.7 nm edge length (**Fig. 2**c and Supplementary Fig. 17). This peak can be explained by the fact that the average *OH binding energy on (111) sites for intermetallic particles increases with particle size and crosses over the volcano plot peak at about 2.7 nm (Supplementary Fig. 18). The predicted specific activity eventually converges to that of the extended $Pt_{29}Ni_7$(111) surface, which is predicted to be about 24 times that of commercial Pt/C (**Fig. *2*c**). Thus in the limit of large particle sizes the intermetallic nanoparticles are predicted to be less active than the most active activated disordered particles (**Fig. *2*c**). This observation can be explained by the fact that the second-layer Pt content is predicted to be lower in these intermetallic particles (Supplementary Fig. 16 and Supplementary Table 8) than that in disordered particles (Supplementary Fig. 11 and Supplementary Table 6) due to the dissolution of Ni atoms from the disordered particles. The relatively Pt-rich second layer in the disordered particles increases the strength of *OH adsorption and increases catalytic activity. This suggests that the additional stability that may be gained through the synthesis of intermetallic nanoparticles may come at the cost of slightly reduced activity.

Summary and Conclusions

Computational design of alloy nanocatalysts is challenging due to the need to predict nanoparticle structures, atomic ordering, adsorbate binding energies, adsorbate-adsorbate interactions, and kinetic evolution. We have demonstrated an approach using an accurate surrogate

model trained on DFT calculations to address all of these challenges, enabling the construction of computationally-generated size-composition activity maps for Pt–Ni nanoparticles for the oxygen reduction reaction. The optimal size and composition predicted by these maps are close to those reported experimentally but slightly more Ni rich (before activation), which may be due to the underprediction of the amount of Ni that is lost to dissolution. One possible reason for this underprediction is that density functional theory predicts subsurface vacancies on Pt(111) to be about 1 eV more stable than surface vacancies. This surprising result is likely related to the well-established problems DFT has in predicting accurate Pt vacancy formation energies.

Our analysis of site-specific OH binding energy and turnover frequency on Pt–Ni nanoparticles demonstrates that surface sites with low coordination number (CN<9), such as edge and vertex sites, are highly inactive due to strong OH binding; while surface Pt(111) sites (CN=9) are relatively more active. The fraction of these Pt(111) sites on the surfaces of activated nanoparticles does not grow as quickly as expected with increasing particle size, likely due to the presence of step edges and other defects. In the limit of large particle sizes, the activated, disordered nanoparticles are still predicted to have slightly higher specific activity than intermetallic Pt_3Ni with an $L1_2$-structured second layer due to lower Ni content in the second layer. At smaller particle sizes, well-ordered particles may have an advantage as they are predicted to be more resistant to Ni dissolution and thus may be better able to maintain the (111)-rich octahedral shape. However these predictions may not bear out in practice if Ni dissolution from either the disordered or intermetallic particle is greater than what we have modeled.

The approach we have developed is well suited to study other alloy systems (or multicomponent materials) and other catalytic reactions, especially those for which the binding energies of simple adsorbates have been established as accurate descriptors. The key to modeling these complex

systems is to develop an accurate surrogate model, which has become increasingly feasible through advances in machine learning. Such models enable researchers to address problems with scale and complexity beyond those achievable with purely *ab initio* methods but with comparable accuracy, enabling the rational design of alloy nanocatalysts.

Methods

Density functional theory (DFT) calculations

DFT calculations were run using the Vienna Ab Initio Simulation Package (VASP)[7] and the RPBE exchange-correlation functional.[47] The Ni, Pt_pv_GW, H_GW, and O_GW PBE projector-augmented wave (PAW)[48] potentials provided with VASP were used. VASP was run with accurate precision with a plane wave cutoff energy of 434 eV. The Brillouin zone was sampled using grids generated by the *k*-point grid server[49] with a minimum distance of 46.5 Å between real space lattice points. Spin polarization was taken into account in the calculations and the Methfessel–Paxton method[50] of order 2 was employed to determine electron occupancies with a smearing parameter of 0.2 eV. The convergence criteria for the electronic self-consistent iteration and the ionic relaxation loop were set to be 10^{-4} eV and 10^{-3} eV, respectively.

Calculation of *OH binding energies

The *OH binding energy (ΔE_{OH}) on the surface site, *i*, of a nanoparticle was calculated as

$$\Delta E_{OH} = E_{DFT}\left(\mathrm{NP{+}k^{*}OH}\right) - E_{DFT}\left(\mathrm{NP{+}(k-1)^{*}OH}\right) + 0.5E_{DFT}\left(\mathrm{H_2}\right) - E_{DFT}\left(\mathrm{H_2O}\right), \qquad (1)$$

where $E_{DFT}\left(\mathrm{NP+n^{*}OH}\right)$ is the DFT energy of the nanoparticle with k adsorbed *OH, $E_{DFT}\left(\mathrm{NP+(n-1)^{*}OH}\right)$ is the DFT energy of the same nanoparticle with one *OH on site i removed, and $E_{DFT}\left(\mathrm{H_2}\right)$ and $E_{DFT}\left(\mathrm{H_2O}\right)$ are the DFT energies of gas-phase H_2 and H_2O. By this definition, more negative values of ΔE_{OH} indicate stronger binding between *OH and the surface of the nanoparticle.

Cluster expansion construction

The Pt–Ni–Vacancy cluster expansion included 341 distinct cluster functions and was trained on 201 structures using the Bayesian approach[51] with a multivariate Gaussian prior distribution, resulting in a leave-one-out cross validation (LOO CV) error of 2.2 meV per atom relative to DFT. To predict OH binding energies on the surface of Pt–Ni nanoparticles with varied sizes, compositions, and shapes we constructed a quaternary Pt–Ni–OH@Pt–Vacancy cluster expansion. As catalytic activities were only calculated on structures that had a Pt skin, we were able to include OH in the cluster expansion by defining a dummy species representing a Pt atom bound to OH, which we refer as OH@Pt. The Pt–Ni–OH@Pt–Vacancy cluster expansion included 1302 distinct cluster functions and was trained on 353 structures using the Bayesian approach, resulting in a LOO CV error of 2.3 meV per atom relative to DFT. The details of cluster expansion are provided in the Supplementary Information.

KMC algorithm to predict nanoparticle structures

The Pt–Ni–Vacancy cluster expansion was used in kinetic Monte Carlo (KMC) simulations to predict the atomic structures of Pt–Ni nanoparticles after experimental CV activation. Detailed descriptions of this approach can be found in references 3, 15.

KMC algorithm to predict ORR activities

To evaluate the ORR specific activity of Pt–Ni nanoparticles, we used a standard "rejection-free" KMC algorithm[32, 33] to predict the turnover frequency on each site, here given by the *OH desorption rate. For each KMC step, the only allowed events were adsorption and desorption. We did not model surface diffusion, which should not affect the equilibrium *OH coverage and distribution. Only atoms with coordination numbers larger than 3 and smaller than 10 were considered to be surface atoms. The transition rate for each event is calculated as $e^{\frac{-E_a}{kT}}$, where E_a is the activation free energy for OH to desorb or adsorb. The free energy for adsorption was calculated as a function of the *OH binding energy to ensure that the turnover frequency was consistent with the right (adsorption-limited) leg of the Sabatier volcano as determined by the work of Norskov et al.[52, 53], and the free energy for desorption was similarly calculated to be consistent with the left (desorption-limited) leg. Additional details are provided in the Supplementary Information.

ASSOCIATED CONTENT

Supplementary Information

Theoretical details of the cluster expansion, kinetic Monte Carlo (KMC) simulations to predict ORR activities, Metropolis Mote Carlo simulations, and other supplementary figures and tables are given.

AUTHOR INFORMATION

Corresponding Author

*tmueller@jhu.edu

Author Contributions

The manuscript was written through contributions of all authors.

Notes

The authors declare no competing financial interests.

ACKNOWLEDGMENT

Liang Cao and Tim Mueller acknowledge support from the Office of Naval Research under MURI award N00014-15-1-2681. Computational resources were provided by XSEDE through award DMR-140068 and by the Maryland Advanced Research Computing Center (MARCC). Atomic-scale structural images were generated using VESTA.[54]

REFERENCES

1. Kang Y, Snyder J, Chi M, Li D, More KL, Markovic NM*, et al.* Multimetallic Core/Interlayer/Shell Nanostructures as Advanced Electrocatalysts. *Nano Lett* 2014, **14**(11)**:** 6361-6367.

2. Huang X, Zhao Z, Cao L, Chen Y, Zhu E, Lin Z*, et al.* High-performance transition metal–doped Pt3Ni octahedra for oxygen reduction reaction. *Science* 2015, **348**(6240)**:** 1230-1234.

3. Cao L, Zhao Z, Liu Z, Gao W, Dai S, Gha J*, et al.* Differential Surface Elemental Distribution Leads to Significantly Enhanced Stability of PtNi-Based ORR Catalysts. *Matter* 2019, **1**(6)**:** 1567-1580.

4. Beermann V, Gocyla M, Willinger E, Rudi S, Heggen M, Dunin-Borkowski RE*, et al.* Rh-Doped Pt–Ni Octahedral Nanoparticles: Understanding the Correlation between Elemental Distribution, Oxygen Reduction Reaction, and Shape Stability. *Nano Lett* 2016, **16**(3)**:** 1719-1725.

5. Cui C, Gan L, Heggen M, Rudi S, Strasser P. Compositional Segregation in Shaped Pt Alloy Nanoparticles and Their Structural Behaviour during Electrocatalysis. *Nat Mater* 2013, **12**(8)**:** 765-771.

6. Kohn W, Sham LJ. Self-Consistent Equations Including Exchange and Correlation Effects. *Phys Rev* 1965, **140**(4A)**:** A1133-A1138.

7. Kresse G, Furthmueller J. Efficient Iterative Schemes for Ab initio Total-Energy Calculations Using a Plane-Wave Basis Set. *Phys Rev B* 1996, **54:** 11169-11186.

8. Gan L, Cui C, Heggen M, Dionigi F, Rudi S, Strasser P. Element-Specific Anisotropic Growth of Shaped Platinum Alloy Nanocrystals. *Science* 2014, **346**(6216)**:** 1502-1506.

9. Beermann V, Kühl S, Strasser P. Tuning the Catalytic Oxygen Reduction Reaction Performance of Pt-Ni Octahedral Nanoparticles by Acid Treatments and Thermal Annealing. *J Electrochem Soc* 2018, **165**(15)**:** J3026-J3030.

10. Chen M, Kumar D, Yi C-W, Goodman DW. The Promotional Effect of Gold in Catalysis by Palladium-Gold. *Science* 2005, **310**(5746)**:** 291-293.

11. Wang Y, Cao L, Libretto NJ, Li X, Li C, Wan Y*, et al.* Ensemble Effect in Bimetallic Electrocatalysts for CO2 Reduction. *J Am Chem Soc* 2019, **141**(42)**:** 16635-16642.

12. Cao L, Mueller T. Rational Design of Pt_3Ni Surface Structures for the Oxygen Reduction Reaction. *J Phys Chem C* 2015, **119**(31)**:** 17735-17747.

13. Cao L, Mueller T. Theoretical Insights into the Effects of Oxidation and Mo-Doping on the Structure and Stability of Pt-Ni Nanoparticles *Nano Lett* 2016, **16**(12)**:** 7748-7754.

14. Li C, Raciti D, Pu T, Cao L, He C, Wang C*, et al.* Improved Prediction of Nanoalloy Structures by the Explicit Inclusion of Adsorbates in Cluster Expansions. *J Phys Chem C* 2018, **122**(31)**:** 18040-18047.

15. Jia Q, Zhao Z, Cao L, Li J, Ghoshal S, Davies V*, et al.* Roles of Mo Surface Dopants in Enhancing the ORR Performance of Octahedral PtNi Nanoparticles. *Nano Lett* 2018, **18**(2)**:** 798-804.

16. Li C, Nilson T, Cao L, Mueller T. Predicting activation energies for vacancy-mediated diffusion in alloys using a transition-state cluster expansion. *Phys Rev Mater* 2021, **in press**.

17. Curtarolo S, Morgan D, Ceder G. Accuracy of ab initio methods in predicting the crystal structures of metals: A review of 80 binary alloys. *Calphad* 2005, **29**(3)**:** 163-211.

18. Verga LG, Aarons J, Sarwar M, Thompsett D, Russell AE, Skylaris CK. DFT calculation of oxygen adsorption on platinum nanoparticles: coverage and size effects. *Faraday Discussions* 2018, **208**(0)**:** 497-522.

19. Tan TL, Wang L-L, Johnson DD, Bai K. A Comprehensive Search for Stable Pt-Pd Nanoalloy Configurations and Their Use as Tunable Catalysts. *Nano Lett* 2012, **12**(Copyright (C) 2015 American Chemical Society (ACS). All Rights Reserved.)**:** 4875-4880.

20. Yuge K. Segregation of $Pt_{28}Rh_{27}$ Bimetallic Nanoparticles: A First-Principles Study. *J Phys: Condens Matter* 2010, **22**(24)**:** 245401.

21. Wang X, Wang Z, Zhuang T-T, Dinh C-T, Li J, Nam D-H*, et al.* Efficient upgrading of CO to C3 fuel using asymmetric C-C coupling active sites. *Nat Commun* 2019, **10**(1)**:** 5186.

22. Chou S-W, Lai Y-R, Yang YY, Tang C-Y, Hayashi M, Chen H-C*, et al.* Uniform size and composition tuning of PtNi octahedra for systematic studies of oxygen reduction reactions. *J Catal* 2014, **309**(0)**:** 343-350.

23. Calle-Vallejo F, Tymoczko J, Colic V, Vu QH, Pohl MD, Morgenstern K*, et al.* Finding optimal surface sites on heterogeneous catalysts by counting nearest neighbors. *Science* 2015, **350**(6257)**:** 185.

24. Calle-Vallejo F, Martínez JI, García-Lastra JM, Sautet P, Loffreda D. Fast Prediction of Adsorption Properties for Platinum Nanocatalysts with Generalized Coordination Numbers. *Angew Chem, Int Ed* 2014, **53**(32)**:** 8316-8319.

25. Jinnouchi R, Asahi R. Predicting Catalytic Activity of Nanoparticles by a DFT-Aided Machine-Learning Algorithm. *J Phys Chem Lett* 2017, **8**(17)**:** 4279-4283.

26. Bartók AP, Kondor R, Csányi G. On representing chemical environments. *Phys Rev B* 2013, **87**(18)**:** 184115.

27. Sanchez JM, Ducastelle F, Gratias D. Generalized Cluster Description of Multicomponent Systems. *Phys A (Amsterdam, Neth)* 1984, **128**(1–2)**:** 334-350.

28. Zhao Z, Chen C, Liu Z, Huang J, Wu M, Liu H*, et al.* Pt-Based Nanocrystal for Electrocatalytic Oxygen Reduction. *Adv Mater* 2019, **0**(0)**:** 1808115.

29. Viswanathan V, Hansen HA, Rossmeisl J, Nørskov JK. Unifying the 2e– and 4e– Reduction of Oxygen on Metal Surfaces. *J Phys Chem Lett* 2012, **3**(20)**:** 2948-2951.

30. Viswanathan V, Hansen HA, Rossmeisl J, Nørskov JK. Universality in Oxygen Reduction Electrocatalysis on Metal Surfaces. *ACS Catal* 2012, **2**(8)**:** 1654-1660.

31. Stamenkovic VR, Fowler B, Mun BS, Wang G, Ross PN, Lucas CA*, et al.* Improved Oxygen Reduction Activity on $Pt_3Ni(111)$ via Increased Surface Site Availability. *Science* 2007, **315:** 493-497.

32. Schulze TP. Efficient kinetic Monte Carlo simulation. *J Comput Phys* 2008, **227**(4)**:** 2455-2462.

33. Serebrinsky SA. Physical Time Scale in Kinetic Monte Carlo Simulations of Continuous-Time Markov Chains. *Phys Rev E* 2011, **83**(3)**:** 037701.

34. Gasteiger HA, Kocha SS, Sompalli B, Wagner FT. Activity Benchmarks and Requirements for Pt, Pt-Alloy, and non-Pt Oxygen Reduction Catalysts for PEMFCs. *Appl Catal, B* 2005, **56**(Copyright (C) 2015 American Chemical Society (ACS). All Rights Reserved.)**:** 9-35.

35. Paulus UA, Wokaun A, Scherer GG, Schmidt TJ, Stamenkovic V, Radmilovic V*, et al.* Oxygen Reduction on Carbon-Supported Pt−Ni and Pt−Co Alloy Catalysts. *J Phys Chem B* 2002, **106**(16)**:** 4181-4191.

36. Choi S-I, Xie S, Shao M, Odell JH, Lu N, Peng H-C*, et al.* Synthesis and Characterization of 9 nm Pt–Ni Octahedra with a Record High Activity of 3.3 A/mgPt for the Oxygen Reduction Reaction. *Nano Lett* 2013, **13**(7)**:** 3420-3425.

37. Yang H, Vogel W, Lamy C, Alonso-Vante N. Structure and Electrocatalytic Activity of Carbon-Supported Pt−Ni Alloy Nanoparticles Toward the Oxygen Reduction Reaction. *J Phys Chem B* 2004, **108**(30)**:** 11024-11034.

38. Zhang C, Hwang SY, Peng Z. Size-dependent oxygen reduction property of octahedral Pt–Ni nanoparticle electrocatalysts. *Journal of Materials Chemistry A* 2014, **2**(46)**:** 19778-19787.

39. Perez-Alonso FJ, McCarthy DN, Nierhoff A, Hernandez-Fernandez P, Strebel C, Stephens IEL*, et al.* The Effect of Size on the Oxygen Electroreduction Activity of Mass-Selected Platinum Nanoparticles. *Angew Chem, Int Ed* 2012, **51**(19)**:** 4641-4643.

40. Shao M, Peles A, Shoemaker K. Electrocatalysis on Platinum Nanoparticles: Particle Size Effect on Oxygen Reduction Reaction Activity. *Nano Lett* 2011, **11**(9)**:** 3714-3719.

41. Mattsson TR, Mattsson AE. Calculating the vacancy formation energy in metals: Pt, Pd, and Mo. *Phys Rev B* 2002, **66**(21)**:** 214110.

42. Nazarov R, Hickel T, Neugebauer J. Vacancy formation energies in fcc metals: Influence of exchange-correlation functionals and correction schemes. *Phys Rev B* 2012, **85**(14)**:** 144118.

43. Leontyev IN, Kuriganova AB, Leontyev NG, Hennet L, Rakhmatullin A, Smirnova NV*, et al.* Size dependence of the lattice parameters of carbon supported platinum nanoparticles: X-ray diffraction analysis and theoretical considerations. *RSC Adv* 2014, **4**(68)**:** 35959-35965.

44. Cao L, Niu L, Mueller T. Computationally generated maps of surface structures and catalytic activities for alloy phase diagrams. *Proc Natl Acad Sci U S A* 2019, **116**(44)**:** 22044-22051.

45. Metropolis N, Rosenbluth AW, Rosenbluth MN, Teller AH, Teller E. Equation of State Calculations by Fast Computing Machines. *J Chem Phys* 1953, **21**(Copyright (C) 2015 American Chemical Society (ACS). All Rights Reserved.)**:** 1087-1092.

46. Lu X-G, Sundman B, A˚gren J. Thermodynamic assessments of the Ni–Pt and Al–Ni–Pt systems. *Calphad* 2009, **33**(3)**:** 450-456.

47. Hammer B, Hansen LB, Nørskov JK. Improved adsorption energetics within density-functional theory using revised Perdew-Burke-Ernzerhof functionals. *Physical Review B* 1999, **59**(11)**:** 7413.

48. Blochl PE. Projector Augmented-Wave Method. *Phys Rev B* 1994, **50**(24)**:** 17953-17979.

49. Wisesa P, McGill KA, Mueller T. Efficient Generation of Generalized Monkhorst-Pack Grids through the Use of Informatics. *Phys Rev B* 2016, **93**(15)**:** 155109.

50. Methfessel M, Paxton AT. High-Precision Sampling for Brillouin-Zone Integration in Metals. *Phys Rev B* 1989, **40**(6)**:** 3616-3621.

51. Mueller T, Ceder G. Bayesian Approach to Cluster Expansions. *Phys Rev B* 2009, **80:** 024103.

52. Rossmeisl J, Logadottir A, Norskov JK. Electrolysis of Water on (Oxidized) Metal Surfaces. *Chem Phys* 2005, **319**(Copyright (C) 2015 American Chemical Society (ACS). All Rights Reserved.)**:** 178-184.

53. Karlberg GS, Rossmeisl J, Norskov JK. Estimations of Electric Field Effects on the Oxygen Reduction Reaction based on the Density Functional Theory. *Phys Chem Chem Phys* 2007, **9:** 5158-5161.

54. Momma K, Izumi F. VESTA: A Three-Dimensional Visualization System for Electronic and Structural Analysis. *J Appl Crystallogr* 2008, **41:** 653-658.

Supplementary Information

Catalytic Activity Maps for Alloy Nanoparticles

Liang Cao[1,2], Tim Mueller[2,*]

[1]Department of Chemistry, Zhejiang University, Hangzhou, Zhejiang 310000, P. R. China

[2]Department of Materials Science and Engineering, Johns Hopkins University, Baltimore, Maryland 21218, United States

1. Cluster expansion

Cluster expansions are generalized Ising models,[1] in which the "spin" variables assigned to each site in an Ising model are replaced by "site" variables that indicate which species (or vacancy) is present at each site.[2, 3] A property of the material (e.g., formation energy) can be expressed as a function of these site variables:

$$F(\mathbf{s}) = V_0 + \sum_{clusters} V_{cluster} \prod_{i \in cluster} \Theta_{b,\mathrm{i}}\left(s_i\right) \qquad [1]$$

where the unknown coefficients, $V_{cluster}$, are known as effective cluster interactions (ECIs), s_i is the site variable at the i^{th} site, $\Theta_{b,i}$ is the b^{th} basis function for the i^{th} site, and V_0 is a constant term representing the ECI for the "empty" cluster. The sum is over clusters of sites, where the number of sites in a cluster may range from 1 to all the sites in the material. When all possible clusters are included in the expansion, the expansion in Eq. [1] is exact. In practice, the ECIs for clusters that contain a large number of sites or sites that are far apart are usually negligible, allowing for the expansion to be truncated to a sum with a finite number of ECIs with little loss of accuracy.

To calculate the ORR activities on Pt–Ni nanoparticles, two cluster expansions models have been developed. The first one is a quaternary Pt–Ni–OH@Pt–Vacancy cluster expansion, which is used to explicitly predict *OH binding energies on the nanoparticle surface and account for the interactions among adsorbed *OH. The second one is the Pt–Ni–Vacancy cluster expansion, which is used to simulate the structural evolution of Pt–Ni nanoparticles using kinetic Monte Carlo and to predict the thermodynamically stable nanoparticles using Metropolis Monte Carlo.

1.1 Pt–Ni–OH@Pt–Vacancy cluster expansion on nanoparticles

The Pt–Ni–OH@Pt–Vacancy cluster expansion was built using an approach similar to one we previously used to build a Pt–Ni–Mo–Vacancy cluster expansion.[4, 5, 6] In the present work, we consider a surface Pt atom and a hydroxyl (OH) adsorbed on its top site as a single dummy species, which is expressed as *OH@Pt. The quaternary Pt–Ni–OH@Pt–Vacancy cluster expansion was generated on an fcc lattice in which each site could be occupied by *OH@Pt, nickel (Ni), platinum (Pt), or a vacancy. Site variable values of 0, 1, 2, and 3 respectively were assigned to these species. The constraint for the dummy species *OH@Pt is that it only can occupy surface sites. For each nanoparticle, atoms with coordination number (nearest-neighboring metal sites) larger than 2 and smaller than 10 are considered to be on surface sites. Pt and Ni Atoms were not permitted to have fewer than 3 nearest neighbors in Monte Carlo simulations. A discrete cosine basis was used to generate the cluster functions, where the b^{th} basis function of the site variable s is given by

$$\Theta_b = \begin{cases} 1 & \text{for b = 0} \\ \sqrt{2}\cos(\pi b(2s + 1) / 8) & \text{for b > 0} \end{cases}, \qquad [2]$$

for $b \in \{0,1,2,3\}$.

For the generation of training data, we reused all training structures that do not contain Mo atoms from the Pt–Ni–Mo–Vacancy cluster expansion[5], leading to an initial set of 151 random clean Pt–Ni particles. By randomly selecting from the pool of 151 clean particles, we created additional 95 random Pt–Ni particles with randomly decorated *OH on surface Pt atoms at varied coverages (35 particles with 0.4 ML, 44 particles with 0.2 ML, 8 particles with 0.15 ML, and 8 particles with 0.1 ML, respectively). All nanoparticles were generated under the constraint that there had to be more than 100 total Pt/Ni atoms in the nanoparticle, as we have found that the inclusion of smaller particles can lead to cluster expansions with poor predictive accuracy for multi-nanometer nanoparticles (probably due to quantum size effects). Nanoparticles that experienced significant reconstruction upon relaxation, defined as an atom traveling more than 75% the nearest-neighbor distance from its initial site, were excluded. All nanoparticles were contained in a cubic cell with a lattice parameter of 28.8

Å. The resulting set of random nanoparticles included 151 clean Pt-Ni nanoparticles without *OH and 95 Pt-Ni nanoparticles with *OH. To improve the accuracy of predicted ORR activities, we included 22 additional Pt–Ni nanoparticles with varied coverages and patterns of adsorbed *OH determined by KMC simulations of ORR activities (see details in section 2) and 7 9-layer Pt–Ni(111) surfaces into the training set.

In addition to these structures, the training data consisted of the pure elements Ni, and Pt in a bulk fcc crystal, vacuum (a lattice containing only vacant sites), and various low-energy structures predicted over the course of this research, for a total of 353 unique structures. These 353 unique training structures included 198 clean Pt–Ni nanoparticles, 145 Pt–Ni nanoparticles with *OH, 7 9-layer Pt–Ni(111) surfaces, 1 Pt bulk, 1 Ni bulk, and 1 vacuum structure. To reduce the prediction error of the cluster expansion[7], the pure elements and vacuum were included twice in the training set. All energies of training set structures were calculated using density functional theory (DFT). Details of the DFT calculations are provided in the Methods section of main body. The effective cluster interactions (ECIs) of the cluster expansions were fit to the DFT-calculated formation energies of fully relaxed nanoparticles relative to the reference states of bulk fcc Ni, bulk fcc Pt, and $0.5E(H_2)$–$E(H_2O)$ for OH. The formation energy can be expressed as

$$\begin{aligned} &FE_{DFT}\left(\mathrm{Pt_mNi_n{}^*OH_k}\right) \\ &= E_{DFT}\left(\mathrm{Pt_mNi_n{}^*OH_k}\right) - mE_{DFT}\left(\mathrm{Pt}\right) - nE_{DFT}\left(\mathrm{Ni}\right) + k\left[0.5E_{DFT}\left(\mathrm{H_2}\right) - E_{DFT}\left(\mathrm{H_2O}\right)\right], \end{aligned} \quad [3]$$

where $E_{DFT}\left(\mathrm{Pt_mNi_n{}^*OH_k}\right)$ is the total DFT energy of the Pt–Ni nanoparticle ($\mathrm{Pt_mNi_n}$) with k adsorbed *OH, $E_{DFT}\left(\mathrm{Pt}\right)$ and $E_{DFT}\left(\mathrm{Ni}\right)$ are the DFT energies of bulk fcc Pt and Ni per atom, and $E_{DFT}\left(\mathrm{H_2}\right)$ and $E_{DFT}\left(\mathrm{H_2O}\right)$ are the DFT energies of gas-phase H_2 and H_2O. Our choice of H_2(g) and H_2O(g) as reference states avoids potential errors in the calculation of the energy of O_2(g) and allows for more direct comparisons with previous calculations.[8]

The Pt–Ni–OH@Pt–Vacancy cluster expansion was truncated to include the empty cluster, the one-body (point) cluster, all 2-body clusters up to the seventh-nearest neighbor, all 3-body clusters up to the fifth-nearest neighbor, all 4-body clusters up to the third-

nearest neighbor, and 5-, and 6-body clusters up to the second-nearest neighbor, for a total of 1302 symmetrically distinct cluster functions. The ECIs for these cluster functions were fit to the training data using the Bayesian approach with a multivariate Gaussian prior distribution.[9] The inverse of the covariance matrix for the prior, Λ, was diagonal, with elements given by

$$\lambda_{\alpha\alpha} = \begin{cases} 0 & \text{for } n_\alpha = 0 \\ \lambda_1 & \text{for } n_\alpha = 1, \\ \lambda_2 (1 + r_\alpha)^{\lambda_3} e^{\lambda_4 n_\alpha} & \text{for } n_\alpha > 1 \end{cases} \qquad [4]$$

where n_α is the number of sites in cluster function α, r_α is the maximum distance between sites, and the parameters λ_1, λ_2, λ_3, and λ_4 were determined by using a conjugate gradient algorithm to minimize the root mean square leave-one-out cross validation (RMS LOOCV) score, an estimate of prediction error.[10] The final values for these parameters were 1.000×10^{-8}, 9.414×10^{-12}, 4.286, and 2.986 respectively. The resulting cluster expansion had a RMS LOOCV error of 2.3 meV per atom relative to DFT calculations.

1.2 Pt–Ni–Vacancy cluster expansion on nanoparticles

The Pt–Ni–Vacancy cluster expansion was built by removing the dummy species (*OH@Pt: surface Pt atom adsorbed with *OH) from Pt–Ni–OH–Vacancy cluster expansion, removing the training structures containing adsorbed *OH, and removing the 9-layer Pt–Ni(111) slabs. The number of structures in the resulting training set is 201. The final values of fitting parameters in Eq. [4] were 1.000×10^{-8}, 9.414×10^{-9}, 4.286, and 2.986, respectively. The resulting cluster expansion had a RMS LOOCV error of 2.2 meV per atom relative to DFT calculations. This cluster expansion is used to simulate the structural evolution (Ni dissolution and Pt/Ni migration) during the experimental CV activation[6, 11] via kinetic Monte Carlo (KMC) as well as predict the thermodynamically stable Pt-Ni nanoparticles via Metropolis Monte Carlo.[4, 5]

2. Assessment of the accuracy of predicted *OH binding energies

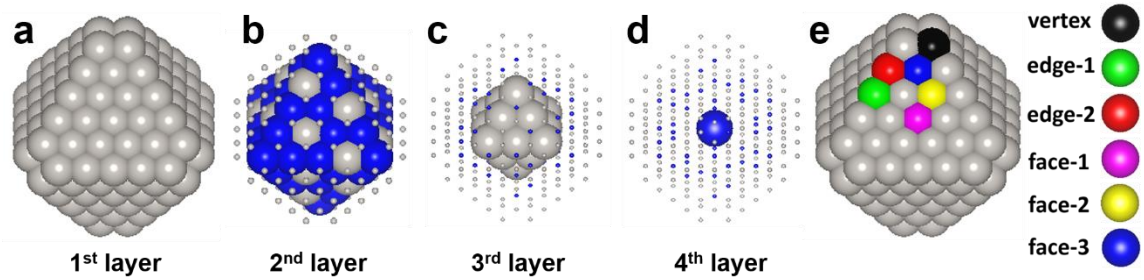

Supplementary Figure 1. (a-d) The layer-by-layer atomic configuration of ground-state $Pt_{178}Ni_{47}$, which is predicted by the cluster expansion in vacuum (reported in our previous work[4, 5]). The 225-atom nanoparticle can be created by truncating one atom on each vertex of perfect octahedral 231-atom nanoparticle. (e) The six types of surface sites by their distinguished numbers of the nearest neighboring Pt/Ni atoms and the 2nd-nearest neighboring atoms.

Supplementary Table 1. The comparison of DFT-calculated and CE-predicted *OH binding energy on varied nanoparticles with a dilute *OH coverage. The surface sites on $Pt_{178}Ni_{47}$ were defined in **Supplementary Figure 1**e. and Pt_{225} was created by replacing all Ni atoms with Pt atoms. Pt_{79}, Pt_{140}, Pt_{225}, Pt_{338}, and Pt_{483} are octahedral nanoparticles with all vertex sites atoms truncated, where "surface-center" sites are the sites furthest to the edges. The generalized coordination number (GCN) was firstly introduced by Calle-Vallejo et al.[12, 13]

particle	surface site	CN	GCN	$\Delta E_{OH,\ DFT}$ /eV	$\Delta E_{OH,\ CE}$ /eV	diff /eV
Pt_{225}	face-1	9	7.5	1.082	0.979	0.103
	face-2	9	7.167	1.006	0.935	0.071
	face-3	9	6.667	0.992	0.902	0.090
	edge-1	7	5.167	0.660	0.640	0.020
	edge-2	7	5.083	0.653	0.614	0.039
	vertex	6	4.083	0.375	0.332	0.043
$Pt_{178}Ni_{47}$	face-1	9	7.5	1.322	1.323	–0.001
	face-2	9	7.167	1.293	1.200	0.093
	face-3	9	6.667	1.077	1.046	0.031
	edge-1	7	5.167	0.878	0.792	0.086
	edge-2	7	5.083	0.762	0.712	0.050
	vertex	6	4.083	0.458	0.459	–0.001
Pt_{79}	face-center	9	7.5	0.955	0.891	0.064
Pt_{140}	face-center	9	7.5	1.029	0.947	0.082
Pt_{225}	face-center	9	7.5	1.082	0.979	0.103
Pt_{338}	face-center	9	7.5	1.077	0.984	0.093
Pt_{483}	face-center	9	7.5	1.115	0.994	0.121

3. Sabatier volcano relating ΔE_{OH} to activation free energy

In this work, we assume the ORR occurs via the associative mechanism in acidic solution with an applied potential of 0.9 V (vs. the reversible hydrogen electrode, RHE) based on previous studies.[8, 14] The binding energies of three intermediate adsorbates (*OOH, *O and *OH) are linearly related.[15] The activation free energy along the reaction pathway (E_a) is correlated to oxygen binding energy (ΔE_O) through a Sabatier volcano plot.[14, 16, 17] At an applied potential of 0.9 V, *OH is the most stable adsorbate on Pt–Ni surface. Thus we converted the Sabatier volcano as a function of oxygen binding energy to *OH binding energy by using the linear relationships among *OOH, *O, and *OH.[15] Thus the activation free energy is expressed as a function of the *OH binding energy (ΔE_{OH})

$$E_a = -\min(-0.297 + 1.0(\Delta E_{OH} - 1.153), -0.297 + 1.06(1.153 - \Delta E_{OH})). \quad [5]$$

where all energies are given in eV and peak position of Sabatier volcano is $\Delta E_{OH,\,peak}$=1.115 eV. There is a difference between the peak position and OH binding energy on Pt(111) with a 1/4 ML coverage ($\Delta E_{OH,\,Pt(111)}$=1.035 eV), which is ~0.1 eV based on previous theoretical predictions[8, 18, 19], and ~0.135 eV based on experimental measurements.[20] The peak position ($\Delta E_{OH,\,peak}$=1.115 eV) was determined by adding the average of above theoretical and experimental differences, which is (0.1 + 0.135) / 2 ≈ 0.118 eV, to $\Delta E_{OH,\,Pt(111)}$.

4. Kinetic Monte Carlo (KMC) simulation to predict ORR activities

To estimate ORR specific activity, we have developed an approach in which the turnover frequency at each site is determined through a KMC simulation. The site-specific turnover frequency is expressed as

$$\text{turnover frequency} = e^{-E_a/kT}, \quad [6]$$

where E_a is the activation free energy and calculated using the Sabatier volcano at varied *OH coverages.

This approach is similar to the one used in our previous work on Pt–Ni(111) surfaces with one monolayer of adsorbed *O/Vacancy.[17] We use a standard "rejection-free" KMC algorithm [21, 22] in which the only allowed transitions are adsorption and desorption. Each simulation was done on each independent nanoparticle, so the number of possible transition events for each KMC step is actually equal to the number of surface Pt atoms (i.e. 1596 for the intermetallic Pt_3Ni nanoparticle in Fig. 1f). In this work, only surface atoms whose coordination number (nearest-neighboring Pt/Ni atoms) is larger than 3 and smaller than 10 are considered as surface atoms. The transition rates (or turnover frequencies) for the transition events were calculated as $e^{\frac{-E_a}{kT}}$.

Specifically, for an adsorption event,

$$E_a = 0.297 + \max(0,\ 1.06(\Delta E_{OH} - 1.153)), \quad [7]$$

where 1.115 is the peak position ($\Delta E_{OH,\,peak}$=1.115 eV) of the volcano plot. For a desorption event,

$$E_a = 0.297 + \max(0,\ 1.0(1.153 - \Delta E_{OH})). \quad [8]$$

The maximum of E_a for an adsorption and a desorption event reproduces the equation of Sabatier volcano (Eq. [5]). After each event, the total elapsed "KMC time" was incremented by

$$\Delta t_{KMC} = \left(\frac{1}{R_N}\right) * \ln\left(\frac{1}{u_1}\right) \quad [9]$$

where R_N is the total rate that sum all possible transition events, and u_1 is a uniform random number with $\mu_1 \in (0,1]$. At the end of the run, the ORR specific activity (SA_{KMC}) was then calculated using

$$SA_{\mathrm{KMC}} = SA_0 \left(\frac{\mathrm{n(accepted\ desorption\ events)}}{t_{\mathrm{KMC}}} \right) \quad [10]$$

where SA_0 is a prefactor, n(accepted desorption events) is the number of accepted *OH desorption events, and t_{KMC} is the "KMC time". When SA_0 is the inverse of the number of adsorption sites on the surface of the studied nanoparticle (i.e. 1/1596 for the intermetallic Pt_3Ni nanoparticle in Fig. 1f), then the KMC current agrees with the current calculated from the Sabatier volcano (Eq. [5]) in the limit of dilute coverage of *OH. The above specific activity(SA_{KMC}) can be converted to mass activity (MA_{KMC}) by multiplying the ratio of the number of surface Pt atoms ($N_{Pt,\,surface}$) to the number of total Pt atoms (N_{Pt}) for a particle.

$$\mathrm{SA}_{\mathrm{KMC}} = \frac{I}{N_{Pt,\,surface}} \quad [11]$$

$$MA_{\mathrm{KMC}} = \frac{I}{N_{Pt}} = \frac{\mathrm{SA}_{\mathrm{KMC}} \times N_{Pt,\,surface}}{N_{Pt}}, \quad [12]$$

where I is the hypothetical total current.

To determine the atomic structures, 10 different octahedral Pt–Ni nanoparticles with the same size and same Pt composition were randomly initialized, and 10 parallel KMC simulations of structural evolution (or Metropolis Monte Carlo simulations) were used to generate 10 different snapshots of activated disordered (or intermetallic) nanoparticles. To calculate the specific and mass activities, we ran a KMC simulation on each disordered or intermetallic nanoparticle. For each KMC simulation, the numbers of both equilibration steps and recording steps are 30 times the number of adsorption sites, and the predicted specific and mass activities and errors were average values and standard deviations (SA based on Eq. [10] and MA based on Eq. [12]) over 10 independent KMC runs on 10 nanoparticles.

5. Benchmark of ORR activities of commercial Pt/C

The definitions of specific activity (SA) and mass activity (MA) for a single Pt–Ni particle are expressed in Eq. [11] and Eq. [12]. To simulate the SA and MA of state-of-the-art commercial Pt/C, we chose a cuboctahedron as the shape of pure Pt nanoparticles based on the Wulff construction of Pt demonstrated in the work of Li et al.[23] The size (in diameter length) distribution of commercial Pt/C (**Supplementary Table *2***) was pulled from our previous work.[6] The weighted average values of SA (3.04E-08) and MA (1.21E-08) for commercial Pt/C were calculated according to the following expressions.

$$\langle SA \rangle = \frac{I}{N_{Pt,\,surface}} = \frac{\sum_i I_i \times p_i}{\sum_i n_{Pt,\,surface,\,i} \times p_i} = \frac{\sum_i (SA_i \times n_{Pt,\,surface,\,i}) \times p_i}{\sum_i n_{Pt,\,surface,\,i} \times p_i}; \quad [13]$$

$$\langle MA \rangle = \frac{I}{N_{Pt}} = \frac{\sum_i I_i \times p_i}{\sum_i n_{Pt,\,i} \times p_i} = \frac{\sum_i (SA_i \times n_{Pt,\,surface,\,i}) \times p_i}{\sum_i n_{Pt,\,i} \times p_i}. \quad [14]$$

As shown in **Supplementary Table *2***, for each pure Pt particle with a specific diameter, p_i is its percentage, and $n_{Pt,\,surface,\,i}$ and $n_{Pt,\,i}$ are the number of surface Pt atoms and the number of all Pt atoms.

Supplementary Table 2. The simulated specific activity (SA) and mass activity (MA) of commercial Pt/C with the size (in diameter) distribution of commercial Pt/C pulled from our previous work.[6] The percentage of particles listed for a specific diameter d is the total percentage of particles with the diameters in the range of d±0.275 nm. The nanoparticles with the diameters smaller than 2 nm have not been counted because the KMC-predicted ORR activities are likely to be less accurate at such small sizes due to quantum finite-size effects. The values of SA_i were predicted using the KMC simulations.

cubo-octahedron	size in diameter (nm)	percentage (p_i)	SA_i	MA_i	$n_{Pt,\,surface,\,i}$	$n_{Pt,\,i}$
Pt_{5851}	5.504	0	6.97E-8	1.73E-8	1452	5851
Pt_{4249}	4.954	2.353	6.61E-8	1.79E-8	1148	4249
Pt_{3101}	4.403	1.176	5.40E-8	1.62E-8	930	3101
Pt_{2075}	3.853	5.882	4.78E-8	1.59E-8	690	2075
Pt_{1385}	3.302	14.118	3.54E-8	1.34E-8	524	1385
Pt_{807}	2.752	41.176	2.35E-8	1.01E-8	348	807
Pt_{459}	2.202	35.295	1.45E-8	7.39E-9	234	459
weighted average of SA			3.04E-8			
weighted average of MA				1.21E-8		

Using the Pt–Ni–OH@Pt–Vacancy cluster expansion, the predicted specific activity of Pt(111) on a 12×12 Pt(111) supercell is 1.15E-7 (**Supplementary Table *3***), which is about 3.8 times that of commercial Pt/C (3.04E-8 in **Supplementary Table 2**) and agrees well with experiments (5 – 10 times).[24, 25] The predicted specific activity of the theoretically identified ground state $Pt_{29}Ni_7(111)$ [16] in equilibrium with bulk Pt_3Ni, which we will refer to as "$Pt_{29}Ni_7(111)$", is about 24.0 times that of commercial Pt/C (3.04E-8). The $Pt_3Ni(111)$ catalyst (PNAS) 7-layer surface[17] and $Pt_3Ni(111)$ catalyst (JPCC) 9-layer surface[16] (**Supplementary Table *3***) were cluster-expansion-predicted surfaces closely matching the layer-by-layer Pt compositions of the highly active $Pt_3Ni(111)$ catalyst reported by Stamenkovic et al.[26]

Supplementary Table 3. The predicted specific activities of 7-layer and 9-layer Pt–Ni(111) surfaces compared with the predicted ones of 9-layer Pt(111) and commercial Pt/C provided in **Supplementary Table 2**. The highly active $Pt_3Ni(111)$ surface reported by Stamenkovic et al. is also included. The specific activity simulations of 7-layer, and 9-layer Pt–Ni(111) were conducted on a 12×12(111) supercell with a vacuum thickness of 11-layer, 9-layer Pt/Ni atoms, respectively.

prediction	SA_{KMC}	SA referenced to commercial Pt/C	SA referenced to Pt(111)
Pt(111)	1.15E-7	3.8	1
$Pt_{29}Ni_7(111)$	7.28E-7	24.0	6.3
$Pt_3Ni(111)$ catalyst (PNAS)	6.18E-07	20.3	5.4
$Pt_3Ni(111)$ catalyst (JPCC)	7.10E-07	23.4	6.2
$Pt_{25}Ni_{11}(111)$-a	1.22E-07	4.0	1.1
$Pt_{25}Ni_{11}(111)$-b	9.14E-10	0.03	0.01
experiment	SA (mA/cm^2)	SA referenced to commercial Pt/C	SA referenced to Pt(111)
$Pt_3Ni(111)$ reported by Stamenkovic at al.[26]	18	90	10

Note: $Pt_{25}Ni_{11}(111)$-a and $Pt_{25}Ni_{11}(111)$-b are 9-layer surfaces with a Pt-skin in the 1st layer and ordered Pt_3Ni in the 4th and 5th layers.[16] The 2nd and 3rd layers are 75% and 25% Pt for $Pt_{25}Ni_{11}(111)$-a, and 100% and zero Pt for $Pt_{25}Ni_{11}(111)$-b.

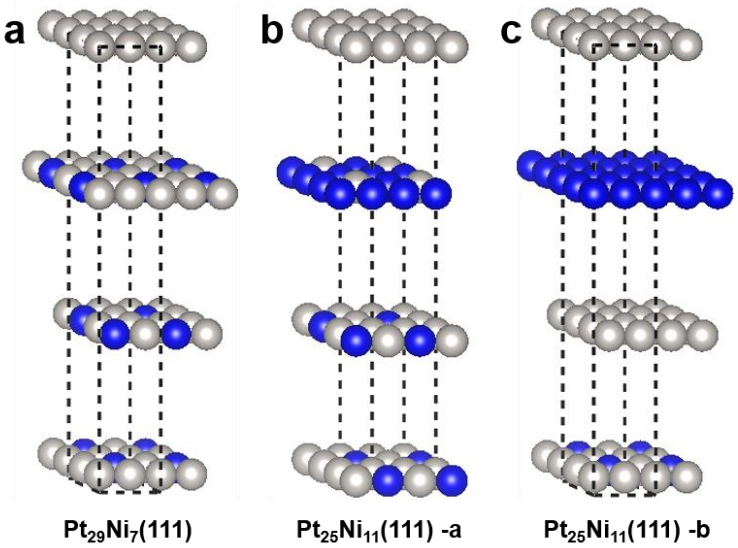

Supplementary Figure 2. The top four layers of three symmetric 9-layer surfaces with a lattice parameter of intermetallic bulk Pt_3Ni. (a, c) ground state surfaces in equilibrium with bulk Pt_3Ni at 0 K predicted in our previous work[16]; (b) a dummy surface with 25%, 75%, and 75% Pt in the 2nd, 3rd, 4th layers, respectively. The grey and blue spheres are Pt and Ni atoms respectively.

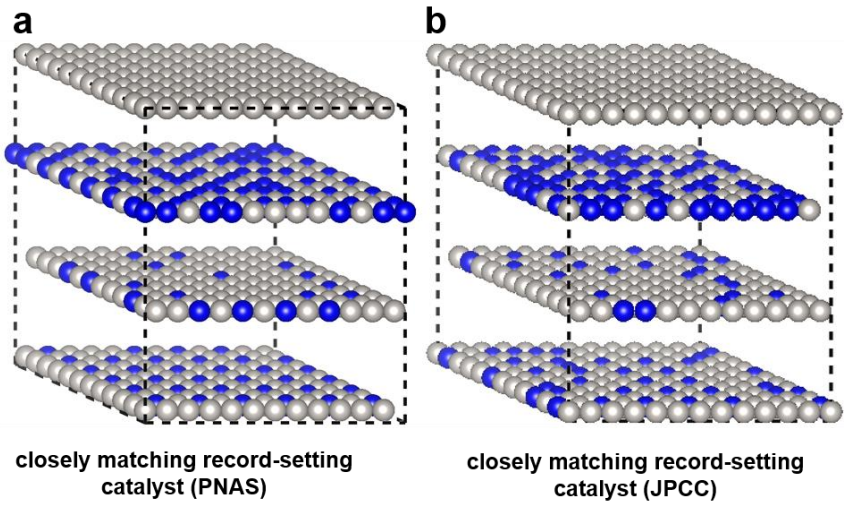

Supplementary Figure 3. The top four layers of two snapshot slabs with a 12 × 12 (111) unit cell from Monte Carlo simulations. (a) a 7-layer snapshot[17] and (c) a 9-layer snapshot[16] matching the layer-by-layer Pt compositions of the highly active $Pt_3Ni(111)$ catalyst reported by Stamenkovic et al.[26] The grey and blue spheres are Pt and Ni atoms respectively.

6. Predicted Ni loss of activated disordered Pt–Ni nanoparticles

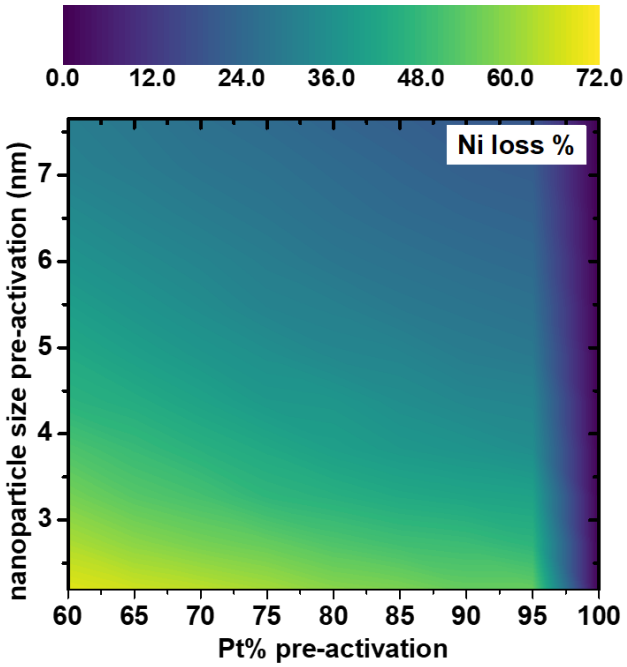

Supplementary Figure 4. Predicted Ni loss of activated disordered Pt–Ni nanoparticles. The x-axis is the Pt composition after KMC with an increment of 5%, and the y-axis is the edge length before KMC (edge length). All specific and mass activity values are referenced to those of simulated commercial Pt/C.

7. Precited specific and mass activities of 3.3 nm disordered particles

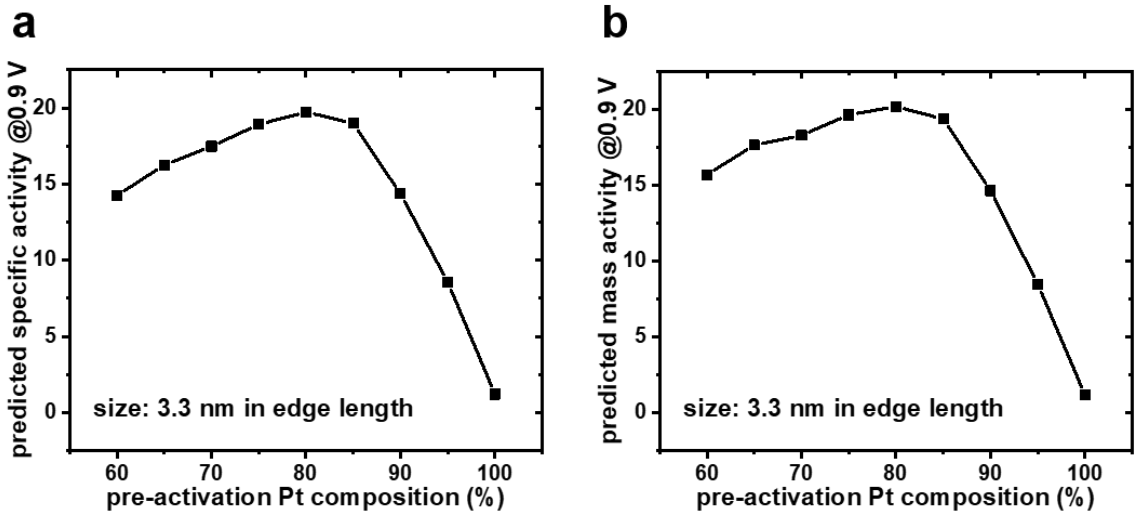

Supplementary Figure 5. The predicted (a) specific activity and (b) mass activity of 3.3 nm activated disorder Pt–Ni particles as a function of pre-activation Pt composition. The values of activities are referenced to those of commercial Pt/C.

8. Predicted average *OH binding energies of post-activated disordered 6175-atom nanoparticles as a function of Pt composition

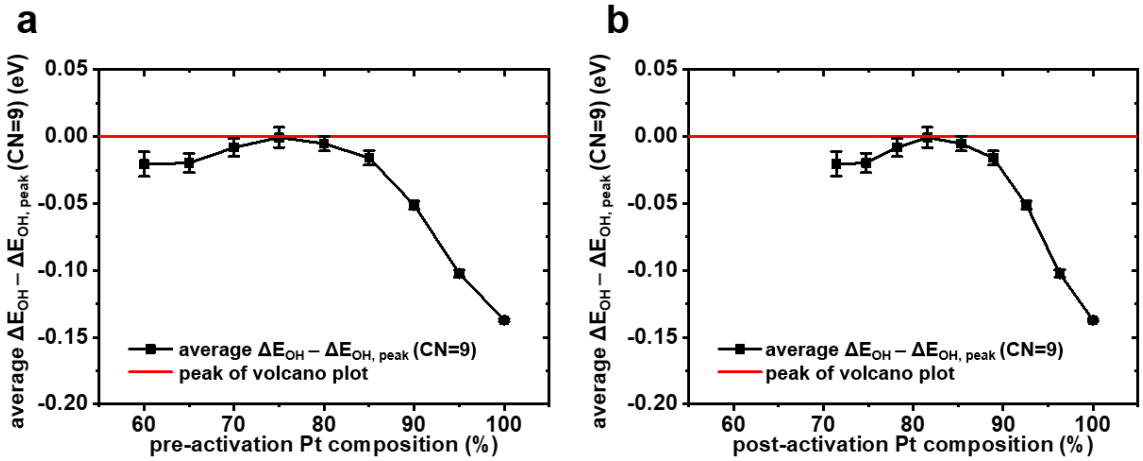

Supplementary Figure 6. The predicted average *OH binding energies, referenced to that of volcano plot peak, on surface sites with coordination number equal to 9 for activated disordered octahedral nanoparticles with initial 6175 atoms as a function of Pt% (a) before KMC (pre-activation) and (b) after KMC (post-activation).

9. Catalytic activity maps as a function of post-activated Pt composition and pre-activated particle size

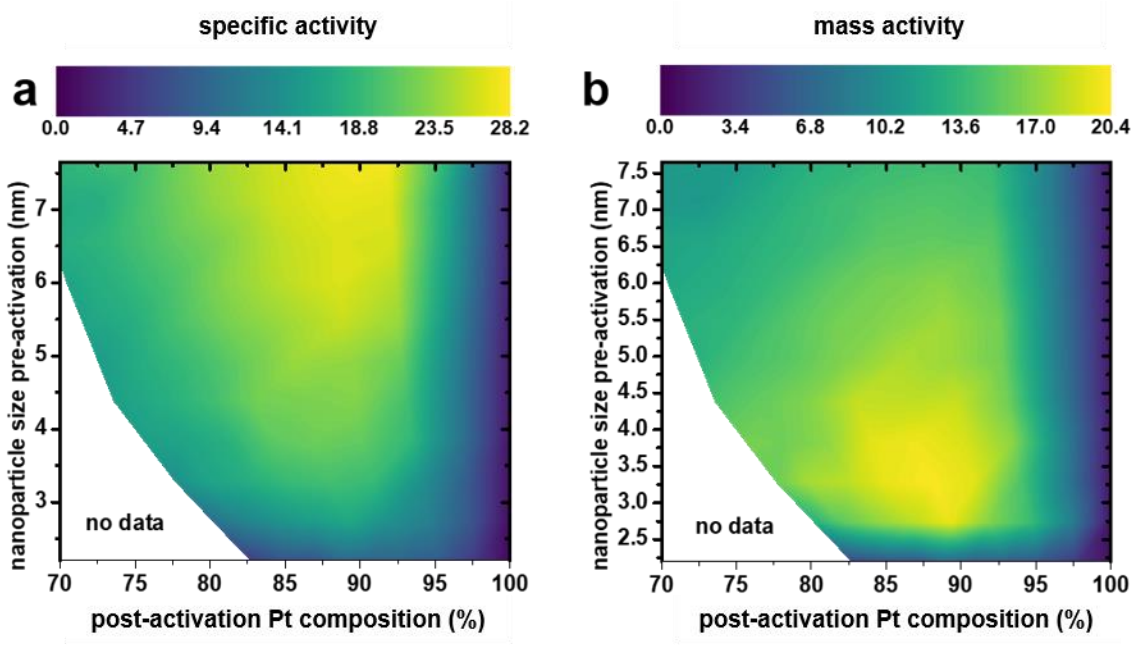

Supplementary Figure 7. Predicted size-composition catalytic activity maps for the ORR. (a) Specific activity and (b) mass activity of activated disordered Pt–Ni nanoparticles. The x-axis is the Pt composition after KMC (post-activation), and the y-axis is the edge length before KMC (pre-activation). All specific and mass activity values are referenced to those of simulated commercial Pt/C.

10. Vacancy formation energies and sub-surface Pt vacancies

Supplementary Table 4. On the (111) surfaces of 225-atom octahedral nanoparticles and Pt(111) as well as representative Pt-rich (111) surfaces, the DFT-calculated vacancy formation energy (VFE) on the 1st and 2nd layers.

structure	position of Pt vacancy	vacancy formation energy (VFE) / eV	difference of VFE between the 2nd and 1st layers / eV
Pt_{225} particle	1st layer	0.990	-1.070
	2nd layer	-0.080	
$Pt_{206}Ni_{19}$ particle	1st layer	1.260	-0.867
	2nd layer	0.393	
Pt(111) with 2×2 supercell	1st layer	0.895	-0.710
	2nd layer	0.184	
Pt(111) with 4×4 supercell	1st layer	1.081	-0.653
	2nd layer	0.428	
$Pt_{29}Ni_7$(111) with 2×2 supercell	1st layer	1.209	-0.562
	2nd layer	0.67	
$Pt_{29}Ni_7$(111) with 4×4 supercell	1st layer	1.291	-0.578
	2nd layer	0.712	

Note: Pt_{225} particle is the octahedral particle with six vertex-site Pt atoms removed (the shape is the same as the $Pt_{178}Ni_{47}$ particle in **Supplementary Figure 1**; $Pt_{206}Ni_{19}$ particle is the Pt_{225} particle with Pt atoms deeper than the 2nd layer replaced by Ni atoms; $Pt_{29}Ni_7$(111) is the surface illustrated in **Supplementary Figure 2**a.

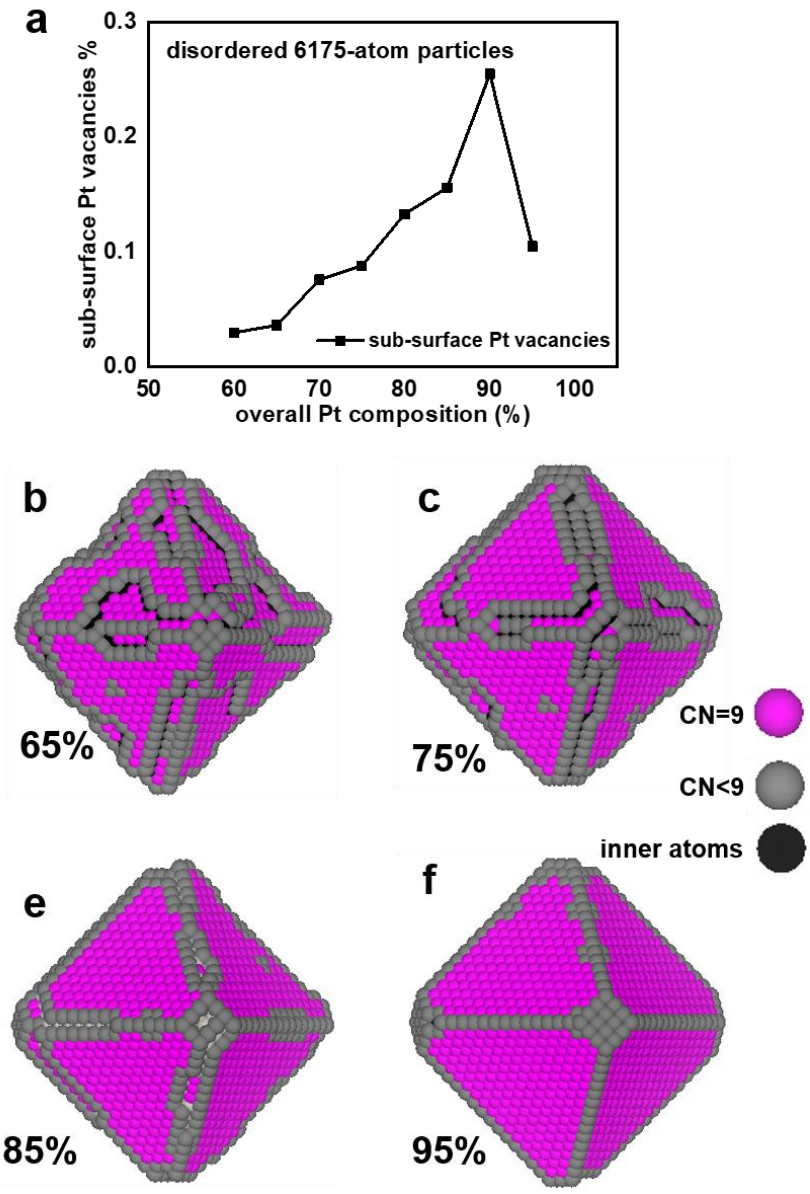

Supplementary Figure 8. The (a) concentration of sub-surface Pt vacancies of activated disordered Pt–Ni particles as a function of the pre-activated Pt composition (b-e) Distribution of surface site coordination numbers of activated disordered particles with pre-activated Pt composition of (b) 65%, (c) 75%, (d) 85%, (e) 95%. In figure b-e, the surface sites on (111) surface with coordination numbers less than 9 have nearest-neighboring sub-surface Pt vacancies.

11. Determination of atomic structures of activated disordered Pt–Ni particles with Pt-rich edges

According to the experimental observation of Pt-rich edges for octahedral Pt−Ni nanoparticles from Strasser et al.'s work[27], we assume that the deposition rate of Pt atoms on edge sites is faster than that on (111) facet sites, and define the degree to which edges are more Pt-rich than (111) facets as *A* using the following equation,

$$A = \frac{\frac{r_{Pt}(e)}{r_{Ni}(e)}}{\frac{r_{Pt}(f)}{r_{Ni}(f)}} = \frac{f_{Pt,e}}{f_{Ni,e}} / \frac{r_{Pt,f}}{r_{Ni,f}}, \qquad [15]$$

where the related notations are defined as follows:

$\frac{r_{Pt}(e)}{r_{Ni}(e)}$ is the deposition rate of Pt referenced to that of Ni on edge sites;

$\frac{r_{Pt}(f)}{r_{Ni}(f)}$ is the deposition rate of Pt referenced to Ni on facet sites;

$f_{Pt,e}$ is the fraction of Pt on the edge sites;

$f_{Ni,e}$ is the fraction of Ni on the edge sites and is equivalent to $\left(1- f_{Pt,e}\right)$;

$f_{Pt,f}$ is the fraction of Pt on the face sites;

$f_{Ni,f}$ is the fraction of Ni on the face sites and is equivalent to $\left(1- f_{Pt,f}\right)$.

Then $f_{Ni,f}$ can be calculated using the following equation:

$$f_{Ni,f} = \frac{2Af_{Ni}}{[f_e + Af_f + (A-1)f_{Ni}] + \sqrt{[f_e + Af_f + (A-1)f_{Ni}]^2 + 4Af_{Ni}(1-A)f_f}}, \qquad [16]$$

where the related definitions are as follows.

f_e is the fraction of total atoms on the edge sites;

f_f is the fraction of total atoms on the face sites and is equivalent to $(1-f_e)$;

f_{Ni} is the total fraction of Ni atoms within the nanoparticles;

f_{Pt} is the total fraction of Pt atoms within the nanoparticles and is equivalent to $(1-f_{Ni})$;

$f_{Ni,e}$ is the fraction of Ni on the edge sites and is equivalent to $\left(f_{Ni}-f_f * f_{Ni,f}\right)/f_e$.

For a 6175-atom octahedral nanoparticle, we define the width of each edge as the three-layers of atoms along the edge and immediately adjacent to the edge, which means there are 3199 atoms on edge sites and 2976 atoms on face sites ($f_e = 3199/6175$ and $f_f = 1-f_e$). The $f_{Ni,f}$ and corresponding distributions of Pt and Ni atoms within the whole Pt–Ni nanoparticles with Pt-rich edges are demonstrated in **Supplementary Table 5** for A=5. Accordingly the Pt and Ni atoms are randomly distributed to initialize the disordered particles, then atomic structures of activated disordered particles are simulated using the kinetic Monte Carlo simulations. The predicted average specific activities over 10 independent snapshot structures for each individual overall Pt composition are demonstrated for *A*=3, 5, 10, and +∞ in **Supplementary Figure 9**. We observed little change in the composition (about 85% Pt for pre-activated particles) predicted to maximize activity across all values of *A*.

Supplementary Table 5. The distributions of Pt and Ni atoms between edge and face sites across the octahedral Pt-Ni nanoparticles with Pt-rich edges for *A*=5.

f_{Pt}	$f_{Ni,f}$	$f_{Ni,e}$	distributions of Pt and Ni atoms			
			$N_{Ni,e}$	$N_{Pt,e}$	$N_{Ni,f}$	$N_{Pt,f}$
0.6	0.5899	0.2234	715	2484	1755	1221
0.65	0.5290	0.1834	587	2612	1574	1402
0.7	0.4639	0.1475	472	2727	1381	1595
0.75	0.3947	0.1154	369	2830	1175	1801
0.8	0.3218	0.0867	277	2922	958	2018
0.85	0.2455	0.0611	196	3003	731	2245
0.9	0.1663	0.0384	123	3076	495	2481
0.95	0.0843	0.0180	58	3141	251	2725

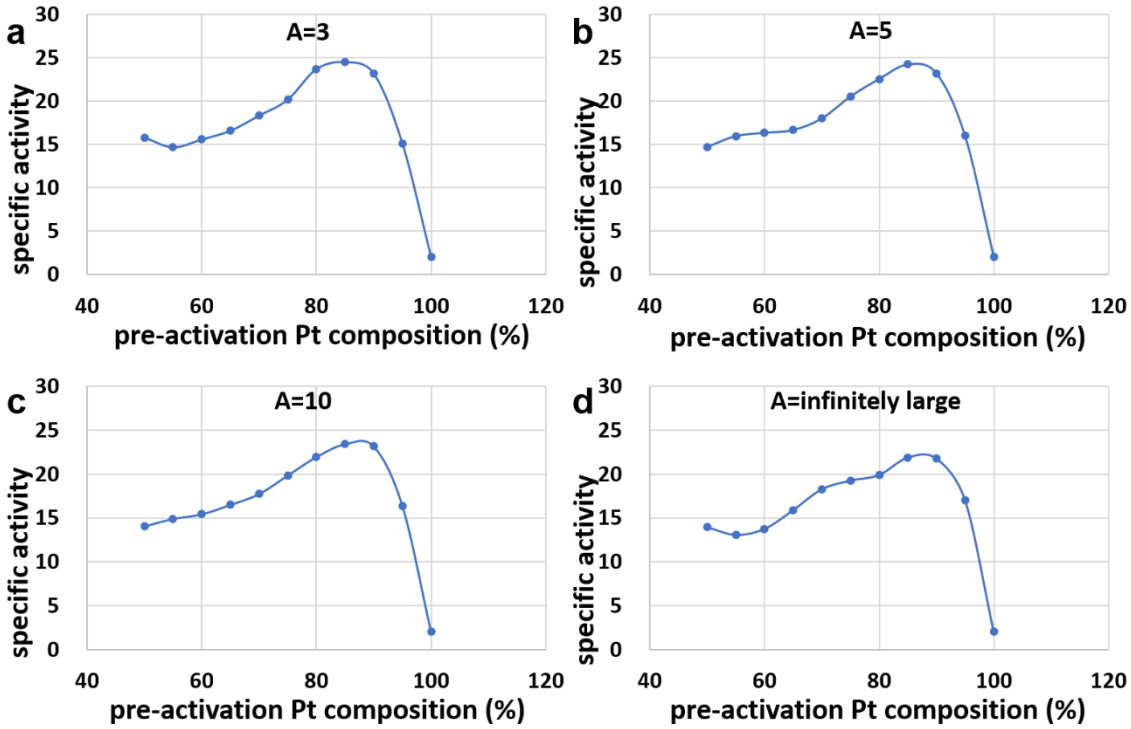

Supplementary Figure 9. The average specific activities (over 10 independent snapshot structures) of activated Pt–Ni particles with Pt-rich edges as a function of pre-activation Pt composition for (a) A=3, (b) A=5, (c) A=10, and (d) A=infinitely large, respectively.

12. Layer-by-layer atomic structures of disordered $Pt_{0.85}Ni_{0.15}$ nanoparticles

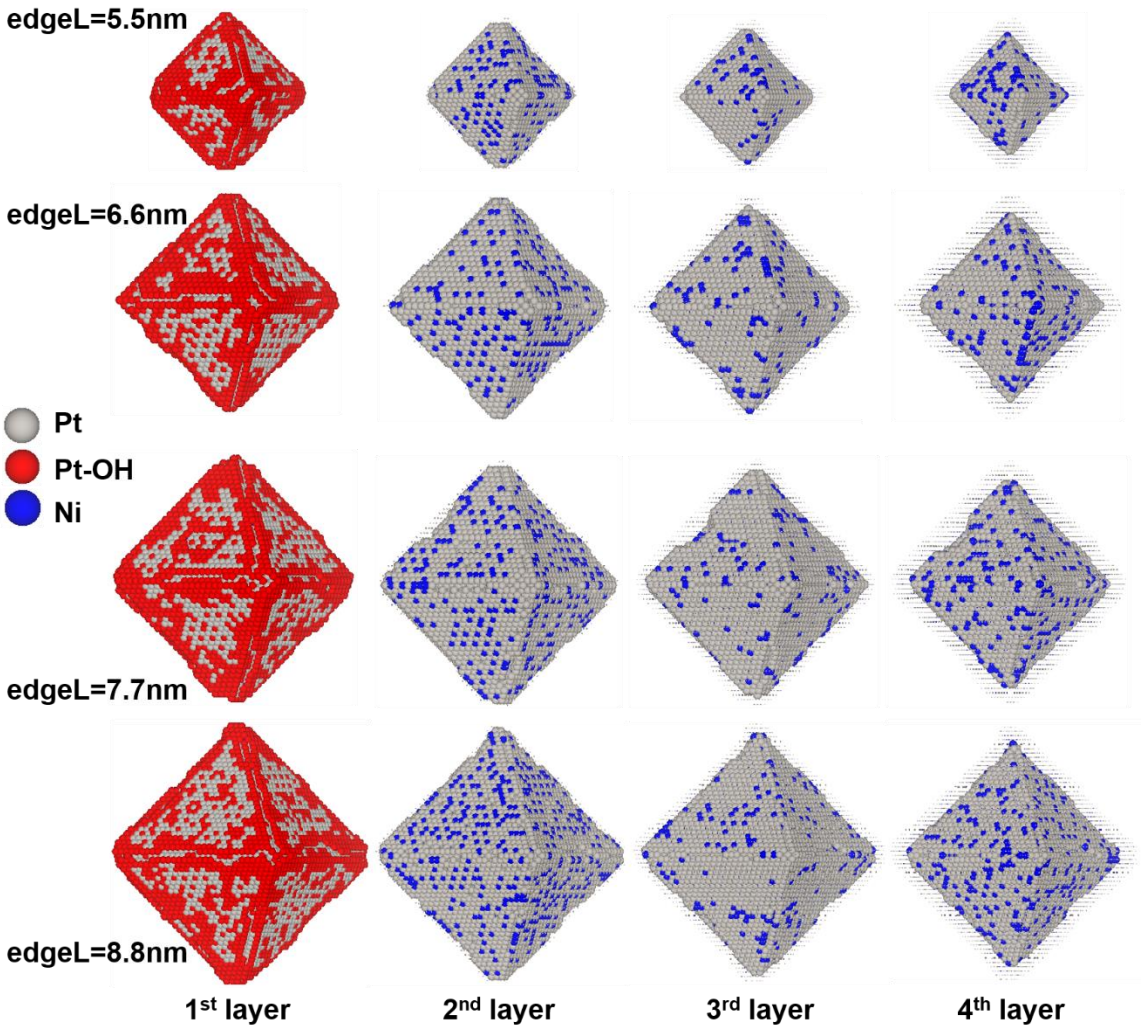

Supplementary Figure 10. The layer-by-layer atomic structures of representative snapshots at 298 K for disordered $Pt_{0.85}Ni_{0.15}$ nanoparticles with adsorbed *OH determined by a KMC run on nanoparticles with edge lengths (before activation) of 5.5 nm, 6.6 nm, 7.7 nm, and 8.8 nm.

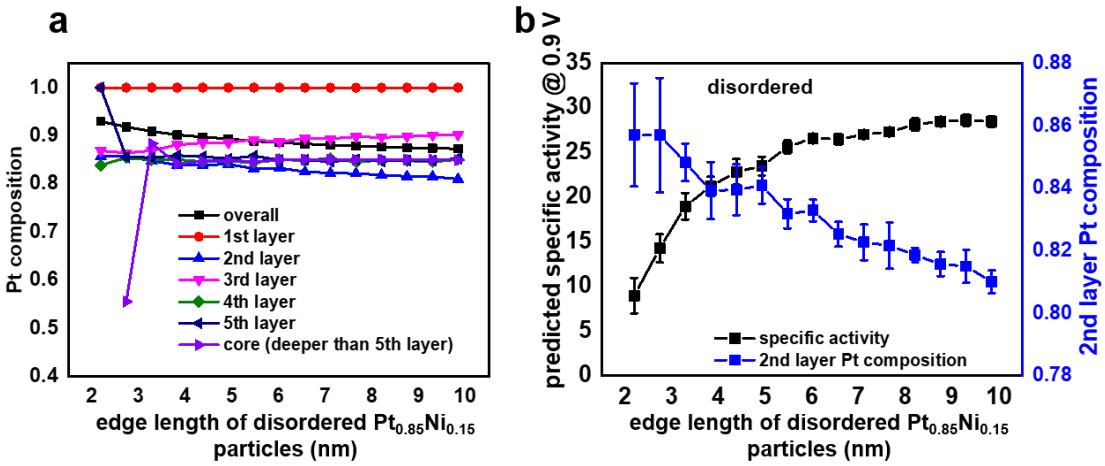

Supplementary Figure 11. The (a) layer-by-layer Pt composition and (b) predicted specific activity compared with the 2nd layer Pt composition for disordered $Pt_{0.85}Ni_{0.15}$ nanoparticles as a function of particle edge length.

Supplementary Table 6. The predicted layer-by-layer Pt composition for disordered $Pt_{0.85}Ni_{0.15}$ nanoparticles at 298 K as a function of edge length from 2.2 nm to 9.9 nm.

size in edge length (nm)	Pt composition (%)					
	overall	1st layer	2nd layer	3rd layer	4th layer	5th layer
2.19	93.0	100	85.7	86.9	83.9	100
2.73	91.9	100	85.7	86.4	85.4	85.6
3.28	90.9	100	84.8	86.9	85.0	85.5
3.83	90.2	100	83.9	88.1	85.1	85.9
4.37	89.7	100	84.0	88.5	84.6	85.7
4.92	89.4	100	84.1	88.6	84.7	85.2
5.47	88.9	100	83.2	89.2	84.4	85.8
6.01	88.6	100	83.3	88.7	85.0	85.0
6.56	88.3	100	82.5	89.5	84.9	85.0
7.11	88.1	100	82.3	89.4	85.3	84.6
7.66	87.9	100	82.2	89.8	84.6	85.1
8.20	87.7	100	81.9	89.7	84.9	84.7
8.75	87.5	100	81.6	89.8	84.8	84.9
9.30	87.4	100	81.5	90.1	84.6	84.9
9.84	87.3	100	81.0	90.2	85.1	85.2

13. Average *OH binding energies on (111) sites with CN=9 for disordered $Pt_{0.85}Ni_{0.15}$ nanoparticles

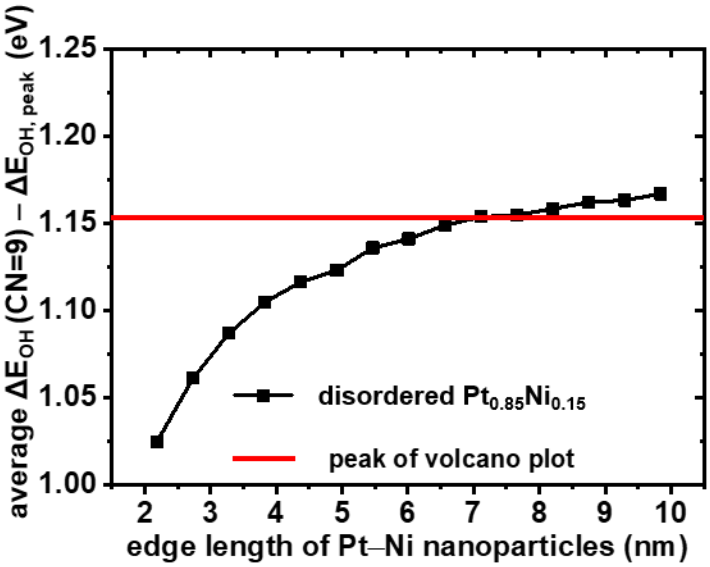

Supplementary Figure 12. Average *OH binding energies on (111) sites with CN=9 for disordered $Pt_{0.85}Ni_{0.15}$ nanoparticles a function of particle size (edge length). The horizontal red line indicates the volcano plot peak.

14. Determination of chemical potentials of Pt and Ni maximizing catalytic activities of intermetallic Pt–Ni particles

To determine the atomic structures of intermetallic Pt_3Ni particles with maximal specific and mass activities, we have run Metropolis Monte Carlo[28] simulations under a grand canonical ensemble within the chemical potential window where bulk ordered Pt_3Ni is stable. To perform above simulations, firstly we refer the chemical potential difference between Pt and Ni as $\mu \equiv \mu(\mathrm{Pt}) - \mu(\mathrm{Ni})$, where reference chemical potentials of the bulk metals are set to zero. Using the same strategy in our previous work[16, 17], the window of μ where bulk Pt_3Ni is stable is between 0.04 eV and 0.50 eV according to the energies of bulk Pt, ordered Pt_3Ni and ordered Pt_2Ni_2 predicted by Pt–Ni–Vacancy cluster expansion in section 1.2. Within the μ window between 0.04 and 0.50 eV (with a grid of 0.025 eV), the thermodynamically stable atomic structures of 6175-atom nanoparticles are simulated using the Metropolis Monte Carlo simulations. The corresponding averaged specific and mass activities over 10 thermodynamic snapshot structures for each chosen value of μ are shown as a function of μ in **Supplementary Figure 13**b. The maximal activities are achieved at $\mu = 0.45\ \mathrm{eV}$ and an overall Pt composition of ~82%. Thus in the present work we will choose $\mu = 0.45\ \mathrm{eV}$ when running Metropolis Monte Carlo simulations to determine the atomic structures of intermetallic Pt–Ni octahedral particles with maximal activities at varied sizes.

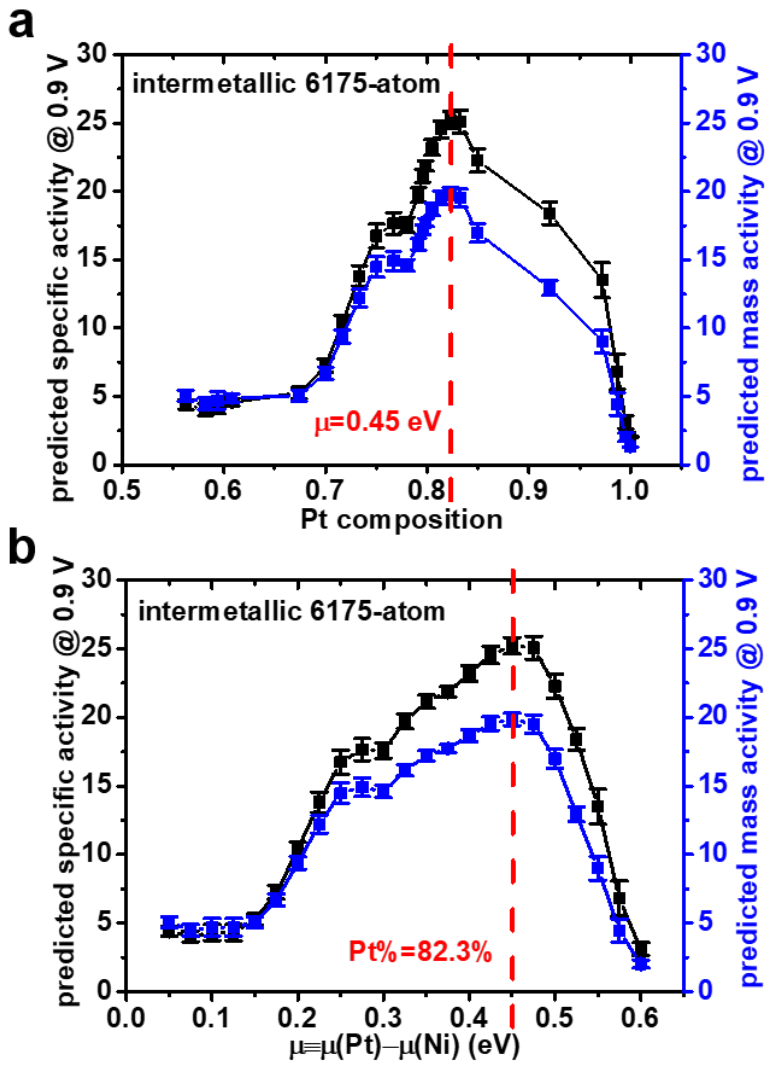

Supplementary Figure 13. The predicted specific and mass activities of intermetallic octahedral nanoparticles with an edge length of 5.5 nm (6175 atoms) as a function of (a) Pt composition and (b) chemical potential difference between Pt and Ni ($\mu \equiv \mu(\mathrm{Pt}) - \mu(\mathrm{Ni})$). The chemical potential window where bulk Pt_3Ni is stable is $\mu \in [0.04, 0.5]\,\mathrm{eV}$, which was predicted based on the Pt–Ni–Vacancy cluster expansion in section 1.2.

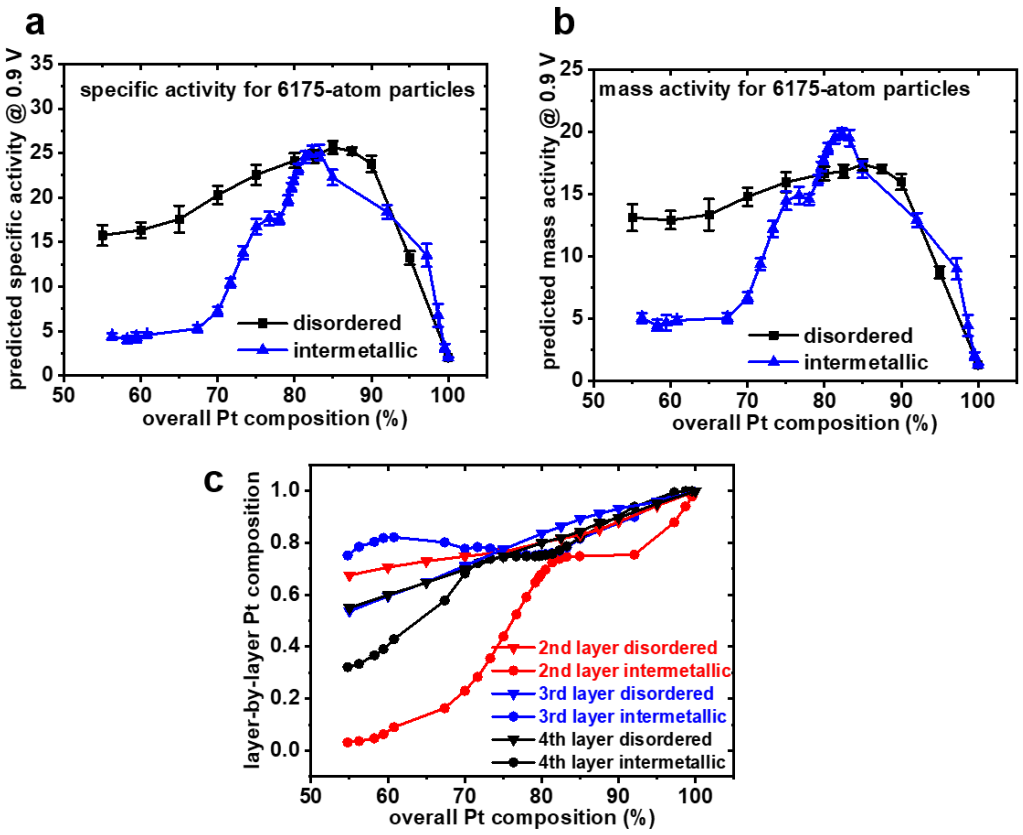

Supplementary Figure 14. The predicted (a) specific activity, (b) mass activity, and (c) layer-by-layer compositions as a function of overall Pt composition for 6175-atom activated disordered and intermetallic nanoparticles. The "6175-atom" for disordered nanoparticles refers to the pre-activated number of total Pt and Ni atoms.

Supplementary Table 7. Layer-by-layer Pt compositions vs. overall Pt composition for 6175-atom disordered and intermetallic nanoparticles. The 6175 atoms for disordered nanoparticles are the pre-activated number of total Pt and Ni atoms.

Pt composition (%)							
6175-atom intermetallic nanoparticles				6175-atom disordered nanoparticles			
overall	2nd layer	3rd layer	4th layer	overall	2nd layer	3rd layer	4th layer
54.76	3.17	75.15	32.14	55	67.55	53.71	54.95
56.24	3.64	78.51	33.37	60	70.60	59.49	59.92
58.22	4.71	80.42	36.67	65	72.95	64.80	64.77
59.41	6.28	81.89	39.07	70	74.83	71.19	69.76
60.79	9.00	82.18	42.90	75	76.55	77.52	74.94
67.38	16.30	80.21	57.79	80	80.06	83.59	79.98
70.00	23.01	77.76	68.26	85	83.18	89.22	84.42
71.66	28.37	78.39	72.16	90	88.11	93.25	89.65
73.31	35.50	77.87	73.88	95	94.31	95.84	95.14
75.02	43.98	76.81	74.56	100	100	100	100
76.69	52.46	75.88	74.80				
78.00	59.07	75.39	74.84				
79.16	64.73	75.16	74.84				
79.60	66.57	75.21	74.91				
79.87	67.67	75.34	74.98				
80.48	69.72	75.69	75.32				
81.36	72.49	76.03	75.74				
82.29	73.82	76.95	77.16				
83.25	74.63	78.19	78.70				
84.95	74.88	81.61	81.93				
92.05	75.48	90.05	93.92				
97.23	87.90	99.40	99.50				

15. Layer-by-layer atomic structures of intermetallic Pt–Ni nanoparticles

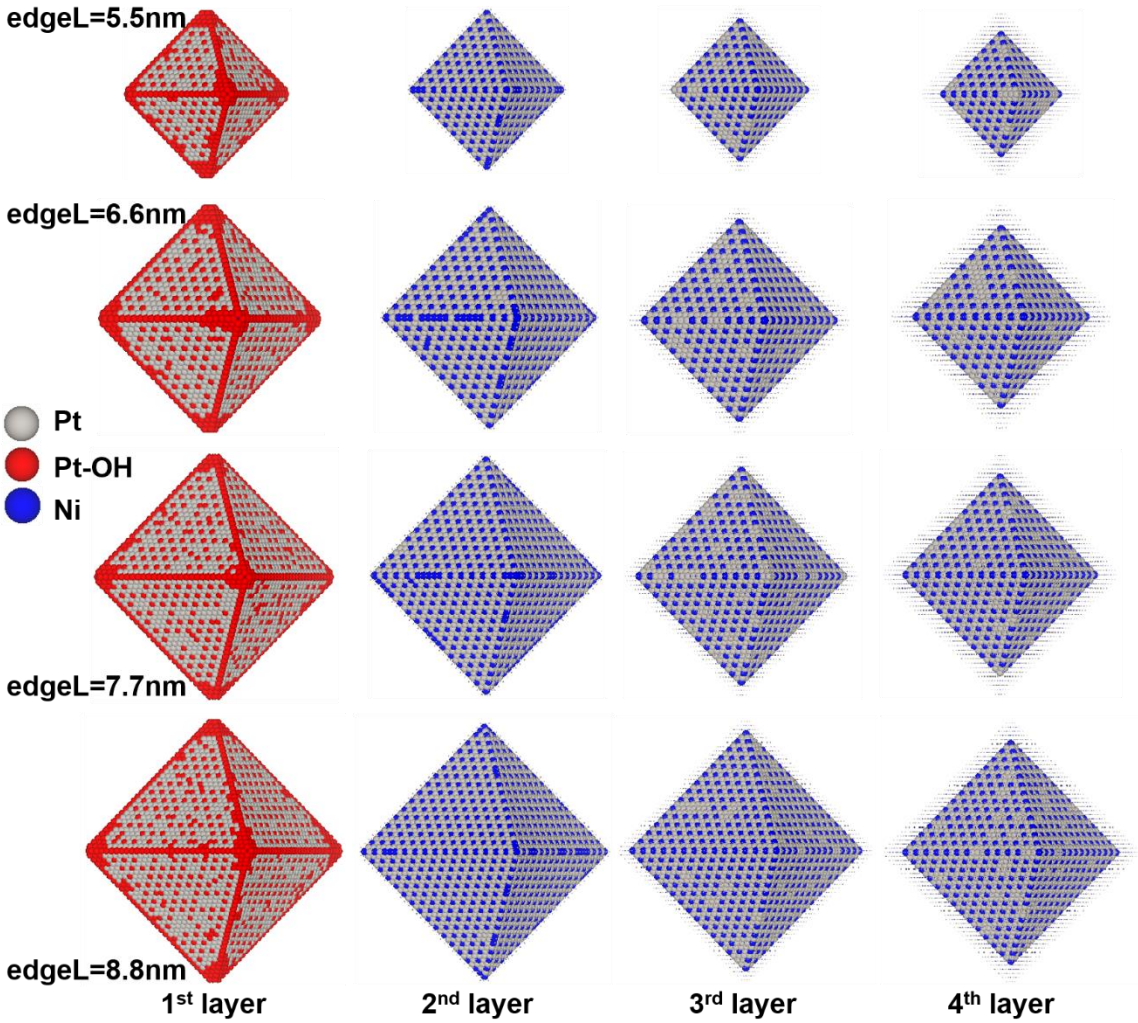

Supplementary Figure 15. The layer-by-layer atomic structures of representative snapshots at 298 K for intermetallic Pt–Ni nanoparticles at μ=0.45 eV with adsorbed *OH determined by KMC run at an edge length of 5.5 nm, 6.6 nm, 7.7 nm, and 8.8 nm. There exists an $L1_2$ structure on subsurface layers.

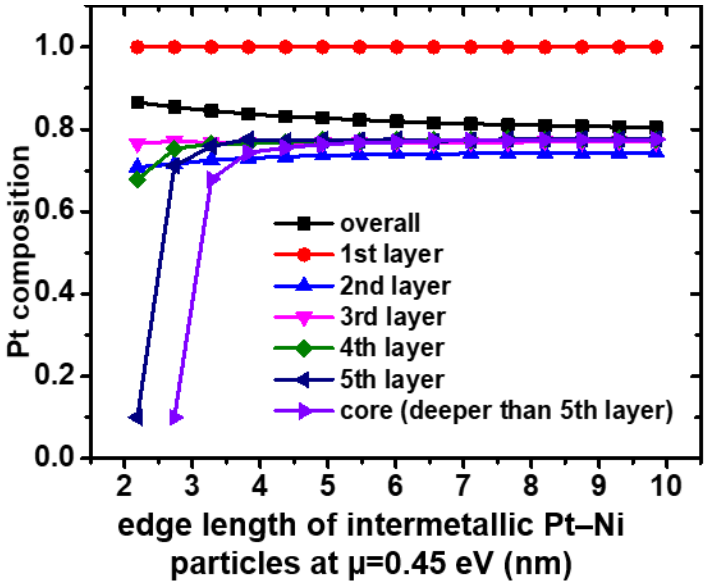

Supplementary Figure 16. The layer-by-layer Pt composition for intermetallic Pt–Ni nanoparticles at μ=0.45 eV as a function of particle edge length.

Supplementary Table 8. The predicted layer-by-layer Pt composition for intermetallic Pt–Ni nanoparticles at μ=0.45 eV at 298 K as a function of edge length from 2.2 nm to 9.9 nm.

size in edge length (nm)	Pt composition (%)					
	overall	1st layer	2nd layer	3rd layer	4th layer	5th layer
2.19	86.6	100	70.8	76.5	67.8	10
2.73	85.4	100	71.6	77.1	75.3	71.1
3.28	84.5	100	72.6	76.8	76.5	75.9
3.83	83.8	100	73.0	76.8	76.6	77.6
4.37	83.1	100	73.4	76.6	76.9	77.2
4.92	82.8	100	73.7	76.9	77.4	77.5
5.47	82.3	100	73.8	76.9	77.2	77.4
6.01	82.0	100	74.1	77.0	77.4	77.6
6.56	81.6	100	73.9	76.7	77.4	77.1
7.11	81.4	100	74.2	76.8	77.3	77.4
7.66	81.1	100	74.2	76.8	77.6	77.6
8.20	81.0	100	74.2	77.0	77.6	77.6
8.75	80.8	100	74.2	77.0	77.6	77.8
9.30	80.6	100	74.3	77.1	77.6	77.6
9.84	80.5	100	74.4	77.0	77.5	77.7

16. Mass activity of disordered and intermetallic nanoparticles as a function of size

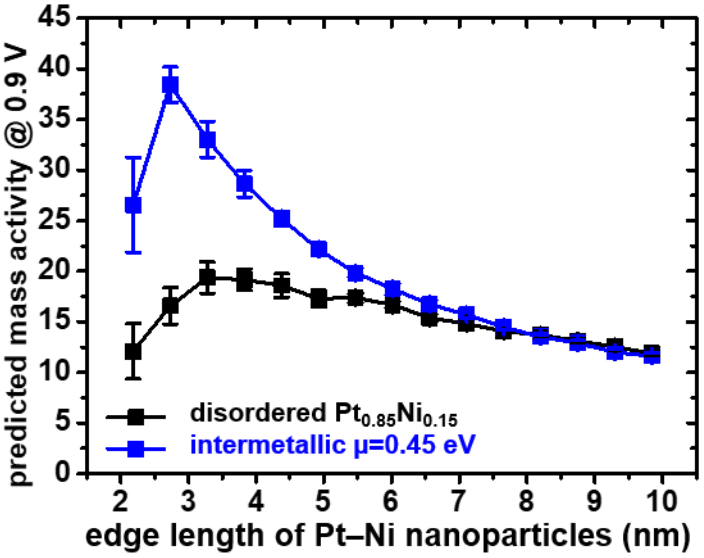

Supplementary Figure 17. Predicted mass activity of disordered $Pt_{0.85}Ni_{0.15}$ nanoparticles and intermetallic Pt–Ni nanoparticles at μ=0.45 eV at 298K as a function of edge length. The mass activity values are referenced to that of simulated commercial Pt/C. The corresponding predicted specific activities are provided in **Fig. 2**c.

17. Average *OH binding energies on (111) sites with CN=9 for disordered $Pt_{0.85}Ni_{0.15}$ and intermetallic Pt–Ni nanoparticles

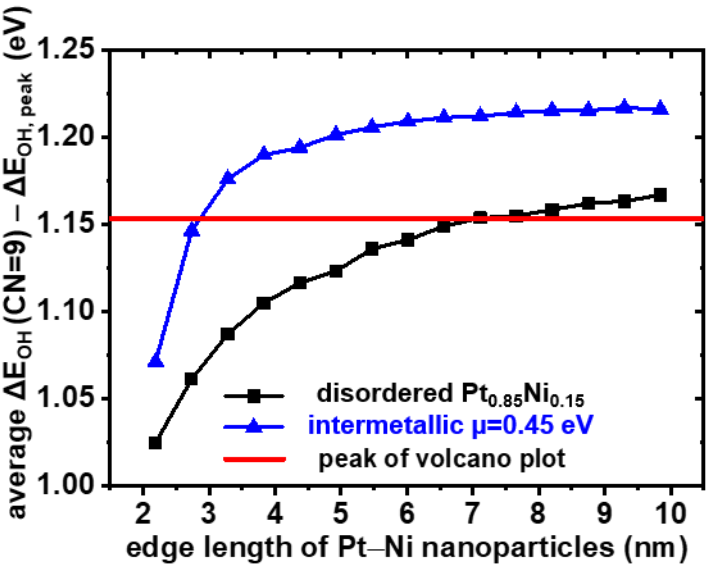

Supplementary Figure 18. Average *OH binding energies on (111) sites with CN=9 for disordered $Pt_{0.85}Ni_{0.15}$ nanoparticles and intermetallic Pt–Ni nanoparticles at μ=0.45 eV as a function of particle size (edge length). The horizontal red line indicates the volcano plot peak.

18. Distribution of OH binding energy and turnover frequencies

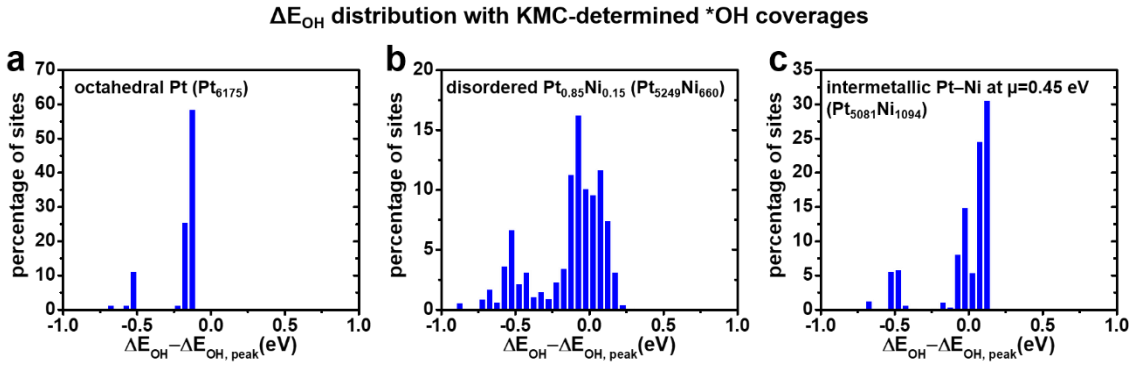

Supplementary Figure 19. Under the KMC-determined *OH coverages, the histograms showing the distribution of average ΔE_{OH} on the surface of three representative nanoparticles in **Fig. 4**a-c: (a) Pt, (b) disordered $Pt_{0.85}Ni_{0.15}$ nanoparticles, and (c) intermetallic Pt–Ni nanoparticles at μ=0.45 eV, respectively. The widths of distribution of ΔE_{OH} in figures (a-c) are [–1.0, 1.0] eV.

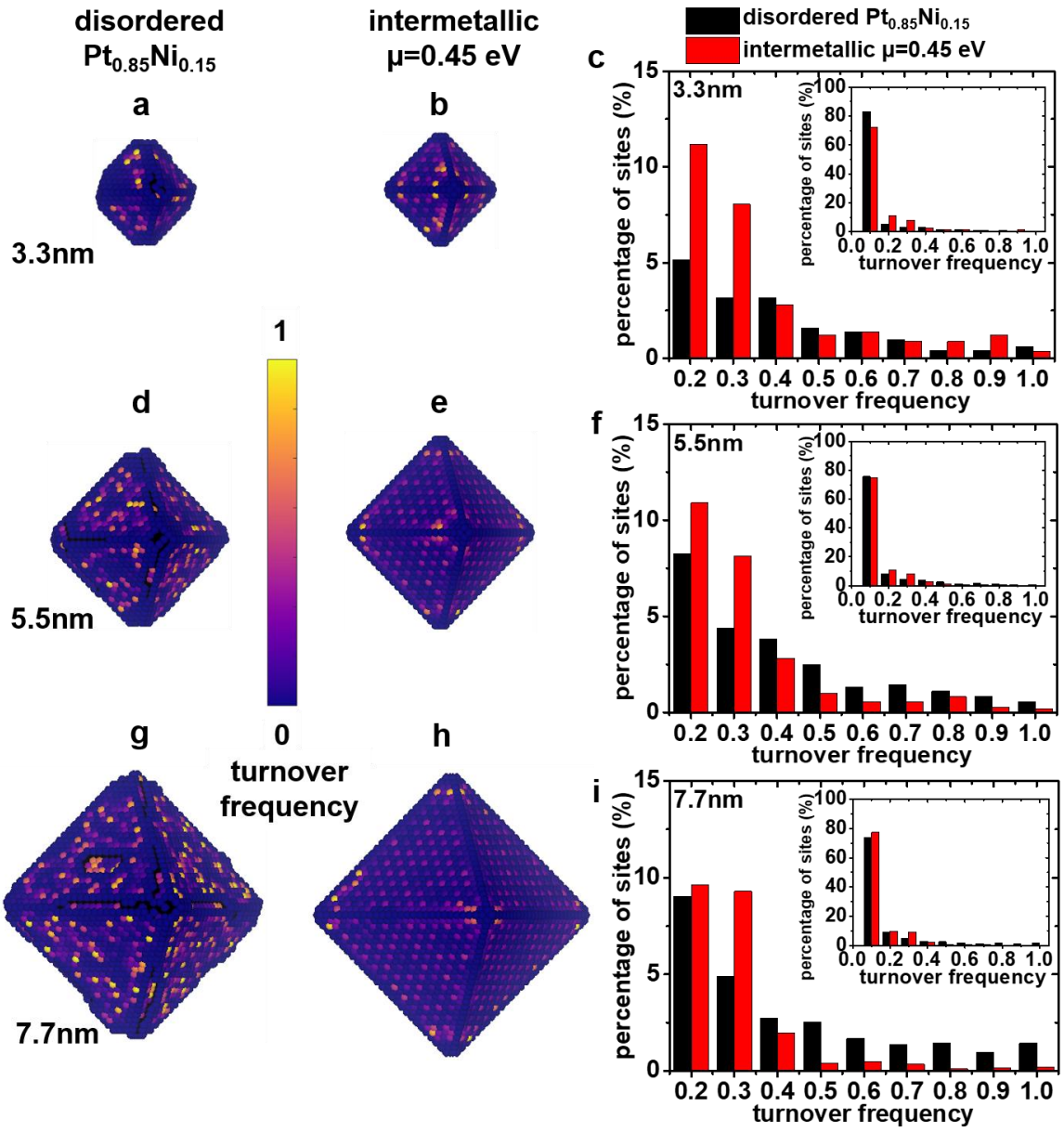

Supplementary Figure 20. Under the KMC-determined *OH coverages, the site-specific average turnover frequency for each surface site of (a, d, g) disordered $Pt_{0.85}Ni_{0.15}$ nanoparticles and (b, e, h) intermetallic Pt–Ni nanoparticles at μ=0.45 eV in an edge length of (a, b) 3.3 nm, (d, e) 5.5 nm, and (g, h) 7.7 nm, respectively. (c, f, i) The corresponding histograms of average turnover frequencies. Both the kinetic Monte Carlo simulations to determine the disordered particles and Metropolis Monte Carlo simulations to determine intermetallic particles were run at 298K. Figures d and e are the same as **Fig. 4**e, f.

Reference

1. Ising E. Beitrag zur Theorie des Ferromagnetismus. *Zeitschrift für Physik* 1925, **31**(1)**:** 253-258.

2. Sanchez JM. Cluster Expansion and the Configurational Theory of Alloys. *Phys Rev B* 2010, **81:** 224202.

3. Sanchez JM, Ducastelle F, Gratias D. Generalized Cluster Description of Multicomponent Systems. *Phys A (Amsterdam, Neth)* 1984, **128**(1–2)**:** 334-350.

4. Huang X, Zhao Z, Cao L, Chen Y, Zhu E, Lin Z*, et al.* High-performance transition metal–doped Pt3Ni octahedra for oxygen reduction reaction. *Science* 2015, **348**(6240)**:** 1230-1234.

5. Cao L, Mueller T. Theoretical Insights into the Effects of Oxidation and Mo-Doping on the Structure and Stability of Pt-Ni Nanoparticles *Nano Lett* 2016, **16**(12)**:** 7748-7754.

6. Jia Q, Zhao Z, Cao L, Li J, Ghoshal S, Davies V*, et al.* Roles of Mo Surface Dopants in Enhancing the ORR Performance of Octahedral PtNi Nanoparticles. *Nano Lett* 2018, **18**(2)**:** 798-804.

7. Mueller T, Ceder G. Exact Expressions for Structure Selection in Cluster Expansions. *Phys Rev B* 2010, **82**(Copyright (C) 2015 American Chemical Society (ACS). All Rights Reserved.)**:** 184107.

8. Norskov JK, Rossmeisl J, Logadottir A, Lindqvist L, Kitchin JR, Bligaard T*, et al.* Origin of the Overpotential for Oxygen Reduction at a Fuel-Cell Cathode. *J Phys Chem B* 2004, **108:** 17886-17892.

9. Mueller T, Ceder G. Bayesian Approach to Cluster Expansions. *Phys Rev B* 2009, **80:** 024103.

10. Van de Walle A, Ceder G. Automating First-Principles Phase Diagram Calculations. *J Phase Equilib* 2002, **23:** 348-359.

11. Cao L, Zhao Z, Liu Z, Gao W, Dai S, Gha J*, et al.* Differential Surface Elemental Distribution Leads to Significantly Enhanced Stability of PtNi-Based ORR Catalysts. *Matter* 2019, **1**(6)**:** 1567-1580.

12. Calle-Vallejo F, Martínez JI, García-Lastra JM, Sautet P, Loffreda D. Fast Prediction of Adsorption Properties for Platinum Nanocatalysts with Generalized Coordination Numbers. *Angew Chem, Int Ed* 2014, **53**(32)**:** 8316-8319.

13. Calle-Vallejo F, Tymoczko J, Colic V, Vu QH, Pohl MD, Morgenstern K*, et al.* Finding optimal surface sites on heterogeneous catalysts by counting nearest neighbors. *Science* 2015, **350**(6257)**:** 185.

14. Karlberg GS, Rossmeisl J, Norskov JK. Estimations of Electric Field Effects on the Oxygen Reduction Reaction based on the Density Functional Theory. *Phys Chem Chem Phys* 2007, **9:** 5158-5161.

15. Rossmeisl J, Logadottir A, Norskov JK. Electrolysis of Water on (Oxidized) Metal Surfaces. *Chem Phys* 2005, **319**(Copyright (C) 2015 American Chemical Society (ACS). All Rights Reserved.)**:** 178-184.

16. Cao L, Mueller T. Rational Design of Pt_3Ni Surface Structures for the Oxygen Reduction Reaction. *J Phys Chem C* 2015, **119**(31)**:** 17735-17747.

17. Cao L, Niu L, Mueller T. Computationally generated maps of surface structures and catalytic activities for alloy phase diagrams. *Proc Natl Acad Sci U S A* 2019, **116**(44)**:** 22044-22051.

18. Rossmeisl J, Karlberg GS, Jaramillo T, Norskov JK. Steady State Oxygen Reduction and Cyclic Voltammetry. *Faraday Discuss* 2008, **140:** 337-346.

19. Viswanathan V, Hansen HA, Rossmeisl J, Nørskov JK. Unifying the 2e– and 4e– Reduction of Oxygen on Metal Surfaces. *J Phys Chem Lett* 2012, **3**(20)**:** 2948-2951.

20. Viswanathan V, Hansen HA, Rossmeisl J, Nørskov JK. Universality in Oxygen Reduction Electrocatalysis on Metal Surfaces. *ACS Catal* 2012, **2**(8)**:** 1654-1660.

21. Schulze TP. Efficient kinetic Monte Carlo simulation. *J Comput Phys* 2008, **227**(4)**:** 2455-2462.

22. Serebrinsky SA. Physical Time Scale in Kinetic Monte Carlo Simulations of Continuous-Time Markov Chains. *Phys Rev E* 2011, **83**(3)**:** 037701.

23. Li C, Raciti D, Pu T, Cao L, He C, Wang C*, et al.* Improved Prediction of Nanoalloy Structures by the Explicit Inclusion of Adsorbates in Cluster Expansions. *J Phys Chem C* 2018, **122**(31)**:** 18040-18047.

24. Gasteiger HA, Kocha SS, Sompalli B, Wagner FT. Activity Benchmarks and Requirements for Pt, Pt-Alloy, and non-Pt Oxygen Reduction Catalysts for PEMFCs. *Appl Catal, B* 2005, **56**(Copyright (C) 2015 American Chemical Society (ACS). All Rights Reserved.)**:** 9-35.

25. Paulus UA, Wokaun A, Scherer GG, Schmidt TJ, Stamenkovic V, Radmilovic V*, et al.* Oxygen Reduction on Carbon-Supported Pt−Ni and Pt−Co Alloy Catalysts. *J Phys Chem B* 2002, **106**(16)**:** 4181-4191.

26. Stamenkovic VR, Fowler B, Mun BS, Wang G, Ross PN, Lucas CA*, et al.* Improved Oxygen Reduction Activity on $Pt_3Ni(111)$ via Increased Surface Site Availability. *Science* 2007, **315:** 493-497.

27. Gan L, Cui C, Heggen M, Dionigi F, Rudi S, Strasser P. Element-Specific Anisotropic Growth of Shaped Platinum Alloy Nanocrystals. *Science* 2014, **346**(6216)**:** 1502-1506.

28. Metropolis N, Rosenbluth AW, Rosenbluth MN, Teller AH, Teller E. Equation of State Calculations by Fast Computing Machines. *J Chem Phys* 1953, **21**(Copyright (C) 2015 American Chemical Society (ACS). All Rights Reserved.)**:** 1087-1092.